## ATMOSPHERIC SCIENCE

# Role of sesquiterpenes in biogenic new particle formation

Lubna Dada[1,2], Dominik Stolzenburg[2,3,4], Mario Simon[5], Lukas Fischer[6], Martin Heinritzi[5], Mingyi Wang[7,8], Mao Xiao[1], Alexander L. Vogel[5], Lauri Ahonen[2], Antonio Amorim[9], Rima Baalbaki[2], Andrea Baccarini[1,10], Urs Baltensperger[1], Federico Bianchi[2], Kaspar R. Daellenbach[1], Jenna DeVivo[7], Antonio Dias[9], Josef Dommen[1], Jonathan Duplissy[2,11], Henning Finkenzeller[12], Armin Hansel[6], Xu-Cheng He[13,2], Victoria Hofbauer[7], Christopher R. Hoyle[1,14], Juha Kangasluoma[2], Changhyuk Kim[15,16], Andreas Kürten[5], Aleksander Kvashnin[17], Roy Mauldin[7,18], Vladimir Makhmutov[17,19], Ruby Marten[1], Bernhard Mentler[6], Wei Nie[2,20], Tuukka Petäjä[2], Lauriane L. J. Quéléver[2], Harald Saathoff[21], Christian Tauber[3], Antonio Tome[22], Ugo Molteni[1,23,24], Rainer Volkamer[13], Robert Wagner[2], Andrea C. Wagner[5], Daniela Wimmer[2], Paul M. Winkler[3], Chao Yan[2], Qiaozhi Zha[2], Matti Rissanen[25,26], Hamish Gordon[7], Joachim Curtius[5], Douglas R. Worsnop[2,27], Katrianne Lehtipalo[2,13], Neil M. Donahue[7], Jasper Kirkby[5,28], Imad El Haddad[1]*, Markku Kulmala[2]*

Biogenic vapors form new particles in the atmosphere, affecting global climate. The contributions of monoterpenes and isoprene to new particle formation (NPF) have been extensively studied. However, sesquiterpenes have received little attention despite a potentially important role due to their high molecular weight. Via chamber experiments performed under atmospheric conditions, we report biogenic NPF resulting from the oxidation of pure mixtures of β-caryophyllene, α-pinene, and isoprene, which produces oxygenated compounds over a wide range of volatilities. We find that a class of vapors termed ultralow-volatility organic compounds (ULVOCs) are highly efficient nucleators and quantitatively determine NPF efficiency. When compared with a mixture of isoprene and monoterpene alone, adding only 2% sesquiterpene increases the ULVOC yield and doubles the formation rate. Thus, sesquiterpene emissions need to be included in assessments of global aerosol concentrations in pristine climates where biogenic NPF is expected to be a major source of cloud condensation nuclei.

## INTRODUCTION

Most of the continental boundary layer receives strong emissions of biogenic volatile organic compounds (BVOCs) from vegetation, especially trees (1). The BVOCs then react with atmospheric oxidants such as hydroxyl radicals (OH), ozone ($O_3$), or nitrate radicals ($NO_3$). This leads to rapid formation of oxygenated vapors with low volatility, particularly from autoxidation processes and monomer-monomer dimerization reactions. However, only a small fraction of the oxidation products with ultralow and extremely low volatilities reach sufficient supersaturation to drive new particle formation (NPF). The newly-formed particles can grow to sizes large enough to influence the atmospheric radiative balance directly or indirectly through acting as cloud condensation nuclei (CCN). Pure biogenic nucleation is an important source of NPF in the preindustrial climate and in pristine regions today (2, 3). Moreover, with the projected further decreases in global $SO_2$ emissions (4–6), pure biogenic nucleation is expected to play an increasingly important role in the future.

Biogenic organic emissions are mostly isoprenoids—isoprene, terpenes, and related compounds—which vary with the type of vegetation and environmental conditions such as stress and predation (7, 8). Among these, sesquiterpenes are a highly reactive class composed of a $C_{15}$ carbon backbone (three isoprene units). β-Caryophyllene is among the most abundant sesquiterpenes emitted by

pine and citrus trees, among other agricultural plants (9–11). Tropical forests, particularly the Amazon, are the largest atmospheric emitters of reactive biogenic volatile isoprenoids (12) and sesquiterpenes (13, 14). Sesquiterpene emissions from trees and shrubs increase as a function of oxidative and thermal stress (10), and a recent study has shown that soil microorganisms also emit sesquiterpenes at a similar rate to the canopy (15). On a global scale, emissions of sesquiterpenes are estimated to be 24 Tg C year$^{-1}$ compared with 91 Tg C year$^{-1}$ for monoterpenes and 465 Tg C year$^{-1}$ for isoprene (13). Although sesquiterpene emissions are lower, they have a higher yield of low-volatility oxidation products and contribute substantially to secondary organic aerosol (SOA) (11, 16–18). Moreover, because of their fast reaction rate with ozone, the potential importance of sesquiterpenes is masked by very low mixing ratios in the atmosphere. In contrast with extensive previous studies of monoterpenes and isoprene, there are relatively few reports on the role of sesquiterpenes in NPF (19–24), and knowledge of their particle nucleation and growth rates is lacking.

## RESULTS

### Cosmics Leaving Outdoor Droplets experiments

Here, in controlled laboratory experiments performed with the Cosmics Leaving Outdoor Droplets (CLOUD) chamber at CERN,

we report the contribution of the sesquiterpene β-caryophyllene ($C_{15}H_{24}$) to particle nucleation and growth resulting from the oxidation of pure BVOC mixtures involving the monoterpene α-pinene ($C_{10}H_{16}$) and isoprene ($C_5H_8$). During the CLOUD11 campaign in fall 2016, we performed a set of pure BVOC NPF experiments including both single precursors and also mixtures (table S1). Pure α-pinene and β-caryophyllene ozonolysis experiments were followed by mixtures of, first, α-pinene and isoprene and, second, α-pinene, isoprene, and β-caryophyllene. For the mixture runs, a molar ratio of 1:6:50 injected precursors (sesquiterpene:monoterpene:isoprene) was maintained to mimic atmospheric emissions of BVOC (*13*). A summary of the experiments and their conditions is provided in table S1.

A typical experiment started with injecting an atmospherically relevant precursor vapor concentration into the chamber in the presence of ozone (Fig. 1 and table S1). The vapor concentrations were then increased together in steps, each of around a factor of two, resulting in increases of the particle formation and growth rates. Pure α-pinene and β-caryophyllene experiments were performed under dark conditions (ozonolysis only); the OH radical concentrations are expected to be ~$1 \times 10^6$ cm$^{-3}$, formed mostly from the ozonolysis reactions (*25*). Mixture runs involving isoprene were performed with ultraviolet (UV) xenon arc lamps (UVH) at 100% intensity to increase the oxidation rate of isoprene by hydroxyl (OH) radicals and allow the formation of dimers (*25*). During these runs, the OH is consumed mostly by isoprene, resulting in OH radical concentrations smaller than $1 \times 10^6$ cm$^{-3}$. Although mixture runs were performed with UV and pure component runs were performed in the dark (without the addition of any OH scavengers), a direct comparison between the two is appropriate, as the reaction of α-pinene and β-caryophyllene with $O_3$ is marginally dominant given that the concentration of $O_3$ is ~$1 \times 10^{12}$ cm$^{-3}$ compared to an OH concentration of less than $1 \times 10^6$ cm$^{-3}$.

The oxidized precursor vapors are known as oxygenated organic molecules (OOMs; see the "Definition of OOM" section in Materials and Methods; figs. S1 and S2). Because the oxidation rates in these experiments are similar to those in the atmosphere, the resulting $RO_2$ radicals have sufficient time to undergo autoxidation and form highly oxygenated products (*26*), forming dimers via $RO_2$ cross-reactions with oxidation products from different BVOCs. OOMs with carbon skeletons exceeding 20 carbon atoms must form from at least one β-caryophyllene unit, given the low abundance of α-pinene trimers at the studied concentrations and

temperatures (figs. S1 and S2). We observe dimer formation involving sesquiterpenes (*11*) equivalent to that previously observed for isoprene and monoterpenes following rapid autoxidation (*2*, *25*, *27*–*31*). These dimers constitute molecules of exceedingly low volatility that can drive particle nucleation.

## DISCUSSION
### Volatility distributions
Figure 2A shows the measured volatility distributions of gas-phase OOMs resulting from the oxidation experiments of pure β-caryophyllene, pure α-pinene, and a mixture of three vapors (β-caryophyllene, α-pinene, and isoprene) in the ratio 1:6:50 (injection mixing ratios). Following Stolzenburg *et al.* (*32*), if a molecule of a specific type ($C_nH_xO_y$) is detected by both the CIMS (chemical ionization mass spectrometer) and PTR3 (proton transfer reaction mass spectrometer), we consider the larger measured concentration by either mass spectrometer as input in the calculations of the volatility distributions as lower concentrations point toward insufficient sensitivity (i.e., a lower than assumed charging efficiency) of the other mass spectrometer. We then combine the measurements into volatility bins (see the "Volatility bin calculation" section in Materials and Methods). Under these experimental conditions [5°C and 40% relative humidity (RH)], all three sets of OOMs comprise mainly relatively volatile organic compounds. Although one-sixth as much β-caryophyllene as α-pinene was flowed into the chamber [yielding lower concentrations in the extremely low volatility organic compound (ELVOC) and LVOC ranges], the ultralow-volatility organic compound (ULVOC) concentrations (compared to total OOM) are similar for all three cases. At this temperature, the signal in the ULVOC and ELVOC range is dominated by molecules detected by the nitrate-CIMS. However, in the LVOC range, notable fractions are only detected by the PTR3, especially for β-caryophyllene oxidation products; this is likely because β-caryophyllene oxidation products fall in that volatility range already with lower degrees of oxygenation (O:C < 0.6; see figs. S3 and S4), where the nitrate-CIMS has reduced sensitivity (*11*). The ULVOC concentration derived from the nitrate-CIMS only is around a factor of two lower that that derived from a combination of nitrate-CIMS and PTR3 (fig. S5).

The mass defect plots in fig. S1 show the carbon numbers associated with each of the systems studied. Pure α-pinene oxidation products are predominantly $C_{10}$ monomers and $C_{20}$ dimers (*30*),

[1]Laboratory of Atmospheric Chemistry, Paul Scherrer Institute, 5232 Villigen, Switzerland. [2]Institute for Atmospheric and Earth System Research (INAR)/Physics, University of Helsinki, FI-00014 Finland. [3]Universität Wien, Fakultät für Physik, 1090 Vienna, Austria. [4]Institute for Materials Chemistry, TU Wien, 1060 Vienna, Austria. [5]Institute for Atmospheric and Environmental Sciences, Goethe University Frankfurt am Main, 60438 Frankfurt am Main, Germany. [6]Institute for Ion Physics and Applied Physics, University of Innsbruck, 6020 Innsbruck, Austria. [7]Center for Atmospheric Particle Studies, Carnegie Mellon University, 5000 Forbes Avenue, Pittsburgh, PA 15213, USA. [8]Division of Chemistry and Chemical Engineering, California Institute of Technology, Pasadena, CA 91125, USA. [9]CENTRA and Faculdade de Ciências da Universidade de Lisboa, Lisboa, Portugal. [10]Laboratory of Atmospheric Processes and their Impact, Ecole Polytechnique Federale de Lausanne, 1015 Lausanne, Switzerland. [11]Helsinki Institute of Physics (HIP)/Physics, Faculty of Science, University of Helsinki, 00014 Helsinki, Finland. [12]Department of Chemistry and CIRES, University of Colorado Boulder, Boulder, CO 80309, USA. [13]Finnish Meteorological Institute, FI-00101 Helsinki, Finland. [14]Institute for Atmospheric and Climate Science, ETH Zurich, 8092 Zurich, Switzerland. [15]School of Civil and Environmental Engineering, Pusan National University, Busan 46241, Republic of Korea. [16]Division of Chemistry and Chemical Engineering, California Institute of Technology, Pasadena, CA 91125, USA. [17]P.N. Lebedev Physical Institute of the Russian Academy of Sciences, 53, Leninskiy Prospekt, Moscow, Russian Federation. [18]Department of Atmospheric and Oceanic Sciences, University of Colorado Boulder, Boulder, CO 80309, USA. [19]Moscow Institute of Physics and Technology (National Research University), 141701 Dolgoprudny, Russian Federation. [20]Joint International Research Laboratory of Atmospheric and Earth System Sciences, School of Atmospheric Sciences, Nanjing University, Nanjing, Jiangsu Province, China. [21]Institute of Meteorology and Climate Research, Karlsruhe Institute of Technology, Hermann-von-Helmholtz-Platz 1, 76344 Eggenstein-Leopoldshafen, Germany. [22]IDL-Universidade da Beira Interior, Covilhã, Portugal. [23]Department of Chemistry, University of California, Irvine, Irvine, CA 92697, USA. [24]Forest Dynamics, Swiss Federal Institute for Forest, Snow and Landscape Research, 8903 Birmensdorf, Switzerland. [25]Aerosol Physics Laboratory, Department of Physics, Tampere University, 33720 Tampere, Finland. [26]Chemistry Department, University of Helsinki, 00014 Helsinki, Finland. [27]Aerodyne Research Inc., Billerica, MA 01821, USA. [28]CERN, CH-1211 Geneva 23, Switzerland.
*Corresponding author. Email: imad.el-haddad@psi.ch (I.E.H.); markku.kulmala@helsinki.fi (M.K.)
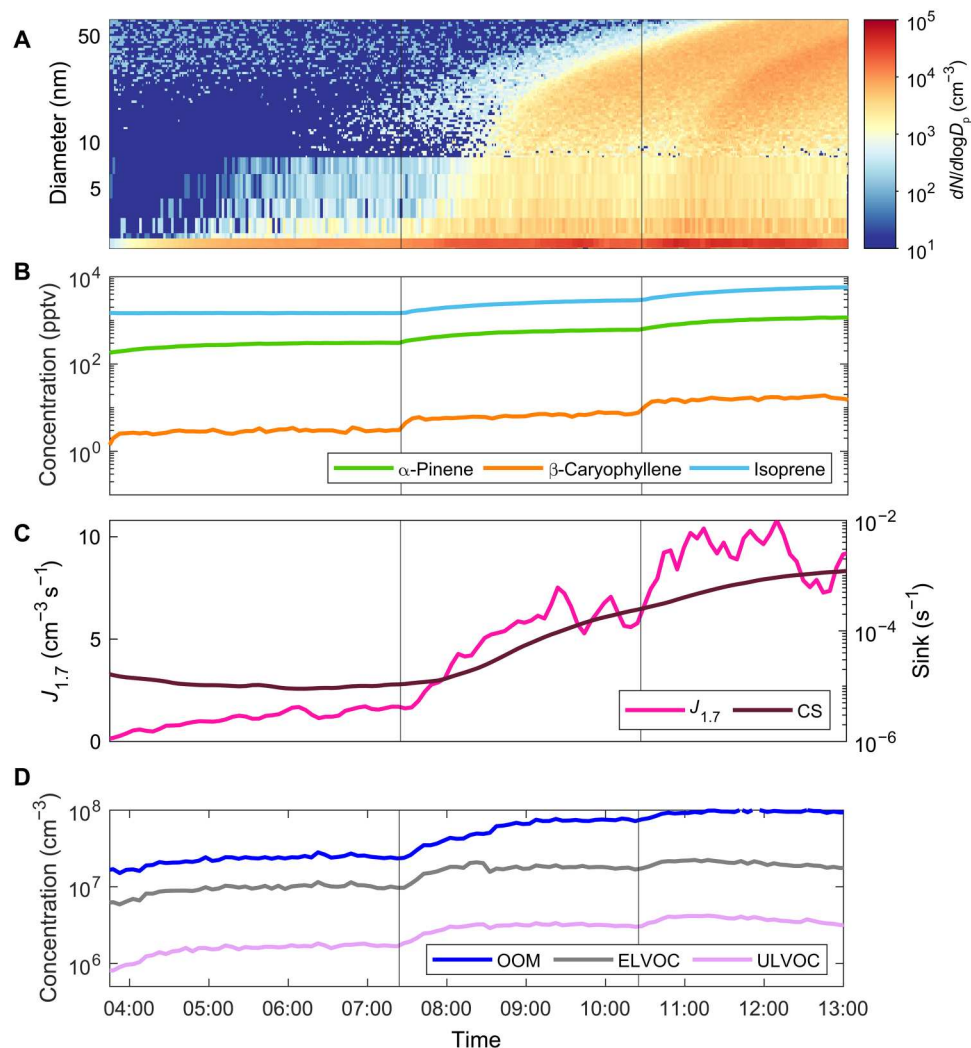
**Fig. 1. Example pure biogenic NPF experiment in CLOUD.** Here, we show a representative mixture run with all three BVOCs (β-caryophyllene, α-pinene, and isoprene) in three concentration steps, with an injected ratio 1:6:50 (β-caryophyllene, α-pinene, and isoprene), 40 ppbv (parts per billion by volume) $O_3$, $T$ = +5°C, relative humidity (RH) = 40%, and full UV lamp intensity; runs 12 to 14 (see table S1). (**A**) The combined particle number size distribution measured using a full suite of particle measuring instruments (see the "Particle counters" section in Materials and Methods). (**B**) Evolution of precursor vapor measured concentrations, α-pinene, β-caryophyllene, and isoprene. The three experimental stages are separated by vertical gray lines. (**C**) Evolution of formation rate of particles with diameter >1.7 nm ($J_{1.7}$) and condensation sink (CS). (**D**) Evolution of oxidation product concentrations measured with $NO_3$-CIMS, total OOMs, extremely low volatility organic compounds (ELVOCs), and ultralow volatility organic compounds (ULVOCs).

while in the presence of isoprene, more $C_{15}$ molecules resulting from α-pinene + isoprene cross-dimer formation are observed (25). The distribution of the monomers from pure β-caryophyllene oxidation peaks around $C_{13}$, $C_{14}$, and $C_{15}$ shown also as a mass spectrum in fig. S2. The dimers resulting from two β-caryophyllene oxidized monomers appear to have a $C_{25-28}$ carbon backbone rather than a $C_{30}$, which could be attributed to loss of carbon atoms during autoxidation. Fragmentation during ozonolysis was already demonstrated for α-pinene (33) and a diterpene (34). However, $C_{30}$ dimers are expected to form under higher β-caryophyllene gas-phase concentrations and lower temperatures (11). The figure also shows the relationship between carbon/oxygen numbers, molecular weight, and volatility.

The increased length of the carbon backbone is translated into ULVOC yields. We find that β-caryophyllene produces, on

average, three times more ULVOCs compared to the α-pinene and isoprene mixture (Fig. 2B). Note that Fig. 2B shows the ULVOC yields as a fraction of the total oxidized β-caryophyllene and α-pinene (see the "OOM yields" section in Materials and Methods). Consistent with the so-called isoprene suppression of NPF (25), adding isoprene to α-pinene reduces the ULVOC yields by a factor of 1.6, but adding even such a small amount of β-caryophyllene (1:6:50 injection mixing ratios) to that mixture restores the ULVOC yields close to the value of pure α-pinene. A dash of sesquiterpene (1.8%) is thus an antidote to NPF suppression by isoprene. As for the contribution of β-caryophyllene to the total OOM production rate (see Eq. 7), Fig. 2C shows the contribution of each precursor along with a comparable mixture of just α-pinene and isoprene presented by Heinritzi *et al.* (25) (see also Fig. 3). For the mixtures, isoprene dominates the total measured OOM, and
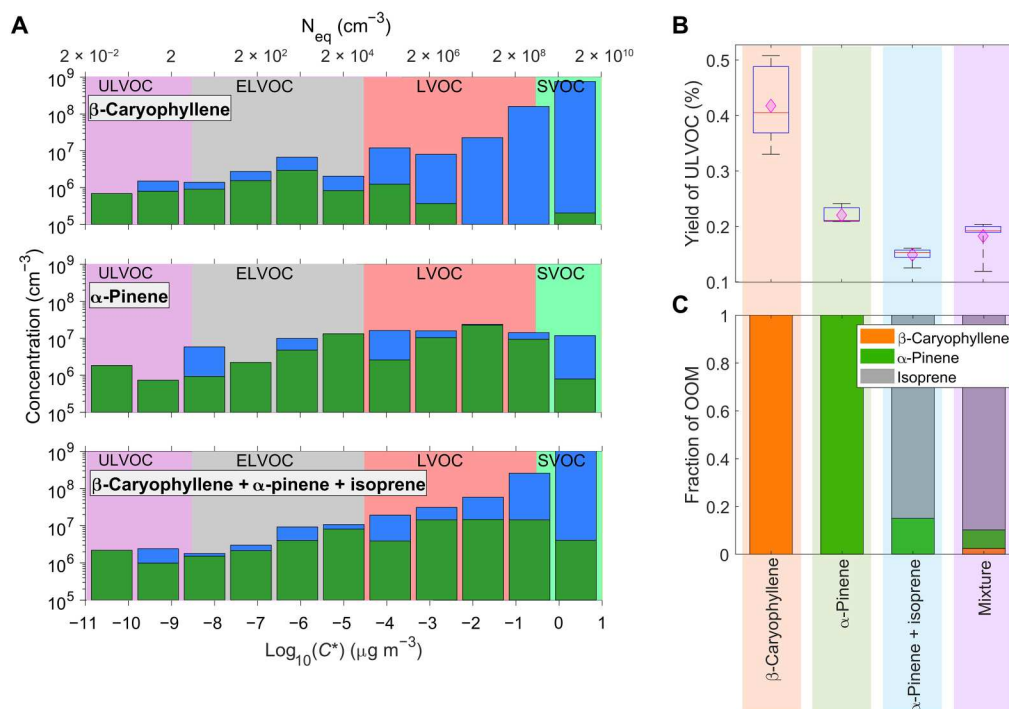
**Fig. 2. ULVOCs produced from pure biogenic nucleation.** (**A**) Volatility distributions, i.e., gas-phase concentration ($cm^{-3}$) versus logarithmic saturation mass concentration ($\log_{10} C_{300}^*$) and saturation number concentration ($cm^{-3}$, converted assuming an average molecular mass of 300 Da) for representative ozonolysis experiments of pure β-caryophyllene (run #10: 0.2 ppbv (parts per billion by volume) injection mixing ratio, top), pure α-pinene (run #4: 1.2 ppbv injection mixing ratio, middle), and a mixture (run #13: 0.2 ppbv β-caryophyllene + 1.2 ppbv α-pinene + 10 ppbv isoprene injected with 40 ppbv ozone and OH radicals, bottom). The experiments were performed at $T = +5°C$ and RH = 40%. The green and blue bars show summed molecular ions measured with two mass spectrometers: a nitrate-CIMS and a PTR3, respectively. The lowest bin is an overflow bin, summing all compounds with lower volatility. The volatility bins are defined at 300 K, shifted, and widened according to their temperature at 278 K. (**B**) Yield of ULVOC produced during pure component runs and in mixtures (see the "OOM yields" section in Materials and Methods). Within each box plot, the red line represents the median of the data and the lower and upper edges of the box represent the 25th and 75th percentiles. Pink diamonds represent the mean of the data. The vertical lines extending from the box represent the minimum and the maximum of the data. (**C**) Contributions of different BVOCs to the overall OOM production rate during pure component runs and with mixtures.

β-caryophyllene has a seemingly negligible contribution (Fig. 2C). However, the ULVOC yield from β-caryophyllene is much higher than any of the other cases (although still <1%).

Most of the ULVOCs are covalently bound accretion products ("dimers") (35), thought to be peroxides (ROOR) formed from cross-reactions between different $RO_2$. A major cause of the isoprene suppression of NPF is the cross-reaction of isoprene-derived ($C_5$) $RO_2$ with monoterpene-derived ($C_{10}$) $RO_2$, which generates $C_{15}$ LVOC ROOR instead of the $C_{20}$ ULVOC ROOR that otherwise is the major nucleating species from terpene oxidation (2, 25). By adding $C_{15}$ $RO_2$ into the reactive mix, sesquiterpenes can stimulate formation of $C_{20}$ dimers (from isoprene and β-caryophyllene) and $C_{25}$ (from α-pinene and β-caryophyllene) dimers (Fig. 3). Furthermore, $C_{30}$ ($C_{26-28}$) dimers from sesquiterpenes easily fall into the ULVOC class (figs. S1 and S2) where nucleation is efficient. Overall, the ULVOC yields in the full 1:6:50 mixture (injected) are similar to pure monoterpene-dominated conditions.

### Particle formation rates
Figure 4A shows that the particle formation rate at 1.7 nm ($J_{1.7}$) as a function of total OOM scales as expected with precursor carbon number: $C_{15}$ (β-caryophyllene) > $C_{10}$ (α-pinene) > $C_5$ (α-pinene + isoprene). The OOM concentration alone cannot explain the difference in the formation rate between the different mixtures. By contrast, as shown in Fig. 4B, ULVOC concentrations measured for the different systems can fully explain the particle formation rates. Plotted as a function of ULVOC concentrations, all precursors drive approximately the same $J_{1.7}$. ULVOCs appear to be the nucleating molecules, with an effective particle formation efficiency approaching 1% of the kinetic limit (discussed in the following section). Here, we also observe that, for the same OOM concentration, the addition of β-caryophyllene in the mixture of α-pinene + isoprene, even at parts per trillion by volume (pptv) levels, enhances $J_{1.7}$ to the same level as of pure α-pinene, overcoming the isoprene suppression effect (25). These results can be explained by the interactions between the reactive $RO_2$ radicals formed after oxidation of each precursor. The $C_{15}$ products formed from sesquiterpenes can, to a large extent, counterbalance the relatively volatile $C_5$ products from isoprene, at least under the conditions explored here (Fig. 3). Similar to pure α-pinene (2) and the mixture of α-pinene + isoprene systems (25), ions play an important role in stabilizing the freshly formed particles from the mixture of α-pinene + isoprene + β-caryophyllene, enhancing the nucleation rate (fig. S6C).

In the presence of nitrogen oxides ($NO_x$), the particle formation rate of the mixture decreases relative to the $NO_x$-free conditions at similar OOM concentrations (Fig. 4C), for experiments at 5°C, 40%
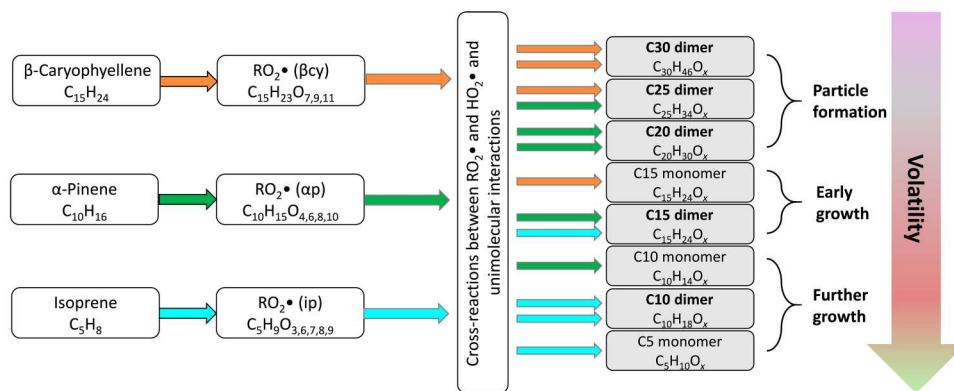
**Fig. 3. Schematic showing how highly oxygenated monomers and dimers are produced by cross-reactions between RO₂ radicals from mixtures of biogenic vapors.** The schematic also illustrates the qualitative nomenclature for the volatility classes at our measurement conditions: ULVOCs drive nucleation; ELVOCs drive growth of even the smallest particles, and LVOCs condense progressively as the particles grow and the Kelvin effect subsides. Here, β-caryophyllene is especially important for NPF and early growth because it has a high yield of the lowest-volatility vapors.

RH, and 40 ppbv O₃. For similar OOM concentrations (e.g., $3 \times 10^7$ cm⁻³; green shade in Fig. 4C), ~25 pptv of NO reduces $J_{1.7}$ by a factor of ~3 (from 1.6 to 0.5 cm⁻³ s⁻¹) and ~75 pptv reduces $J_{1.7}$ by a factor of ~5 (from 1.6 to 0.33 cm⁻³ s⁻¹). The effects of adding NO on the particle formation rates and the volatility distribution of the OOM molecules are shown in figs. S6 and S7. The effect of NOₓ on monoterpene oxidation has been shown previously, in which the formation of accretion products is suppressed in the presence of sufficient NOₓ, resulting in more volatile OOM reducing particle formation rate and growth (36, 37). Hence, the observed decrease in $J_{1.7}$ associated with NOₓ could possibly be attributed to the dimer formation suppression for the mixture and, hence, a shift in the distribution of the oxidation products toward higher volatilities. However, we do not observe a clear decrease in the ULVOC concentration. This is expected as the measurement of organonitrates using the NO₃⁻-based CI-APi-ToF remains challenging and the volatility basis set (VBS) model in the presence of nitrated molecules is subject to large uncertainty (36).

For the biogenic mixture, increasing temperature decreases the particle formation rate as a function of increasing total OOM (fig. S6). However, when plotting $J_{1.7}$ as a function of ULVOC (always expressed for the actual temperature), we find that the ULVOC abundance explains the variability in the formation rate regardless of the temperature (Fig. 4D). The ULVOC to OOM fraction, however, is substantially higher at lower temperatures; this is consistent with the findings of Simon *et al.* (30) and Ye *et al.* (38), who showed that the yield of ULVOC from pure α-pinene experiments decreases with increasing temperature. The effect of RH is only observed at +5°C (278 K), where $J_{1.7}$ may have been enhanced by as much as a factor of 2 at 90% RH and suppressed by a factor of 2 at 5% RH. At +25°C (298 K), no difference in $J_{1.7}$ is observed when RH is increased from 40 to 65% (Fig. 4D).

### Particle growth rates
In addition to causing more efficient particle formation, β-caryophyllene oxidation is expected to cause faster particle growth (per mole of carbon oxidized), consistent with its known high mass yields of SOA (11, 39, 40). Here, we measured the growth rates of particles in the size range between 2.5 and 8 nm for pure β-caryophyllene, α-pinene, α-pinene + isoprene, and the mixture of all 3

BVOCs (Fig. 5, A and B). We find that ELVOC and ULVOC combined are capable of approximately explaining the growth of the small particles between 1.8 and 3.2 nm, assuming kinetically limited condensation (41), while LVOC are, in addition, needed at larger sizes (3.2 to 8 nm) to obtain measured growth rates scattered around the kinetic limit line (see also fig. S8). In addition, we described the growth rate using the different bins of the VBS distribution as shown in Fig. 5C (see fig. S4 for a comparison between measured and modeled volatility results). We mapped the observed vapors into a one-dimensional VBS and then calculated growth rates as a function of size, following the procedure of Stolzenburg *et al.* (32) (see also the "Particle formation and growth rates" section in Materials and Methods). The calculated growth agrees well with the observations, with growth rates accelerating over the observed size range, even as the collisional (kinetically limited) growth rate would decline. The gray contour lines and colors in the plot show the 278-K volatility-class of each bin and its contribution to the total growth rate. The least volatile (ULVOC and ELVOC) products condense almost kinetically at all sizes and show a decreasing contribution with increasing size, whereas the somewhat more volatile LVOC start to contribute substantially above 2 nm as the Kelvin effect subsides, causing the overall growth rate to accelerate with size. This illustrates the qualitative nomenclature for these classes at our measurement conditions: ULVOCs drive nucleation; ELVOCs drive growth of even the smallest particles, and LVOCs condense progressively as the particles grow and the Kelvin effect subsides.

### Generalization of pure biogenic nucleation
Independent of the BVOC mixture studied; whether pure α-pinene, pure β-caryophyllene, α-pinene + isoprene, or a mixture of α-pinene + isoprene + β-caryophyllene; and regardless of the NO concentration, temperature, or RH, we observe a strong correlation between ULVOCs and $J_{1.7}$, as shown in Fig. 3. In Fig. 6A, we show that $J_{1.7}$ closely follows the 1% kinetic limit for ULVOC collisions. The spread that is still observed can almost be entirely attributed to gas-phase measurement uncertainties. Such an observation can be attributed to the instability of ULVOC-ULVOC clusters, which could be structurally strained given their bulkiness, and hence are subject to evaporation. On average, three ULVOC
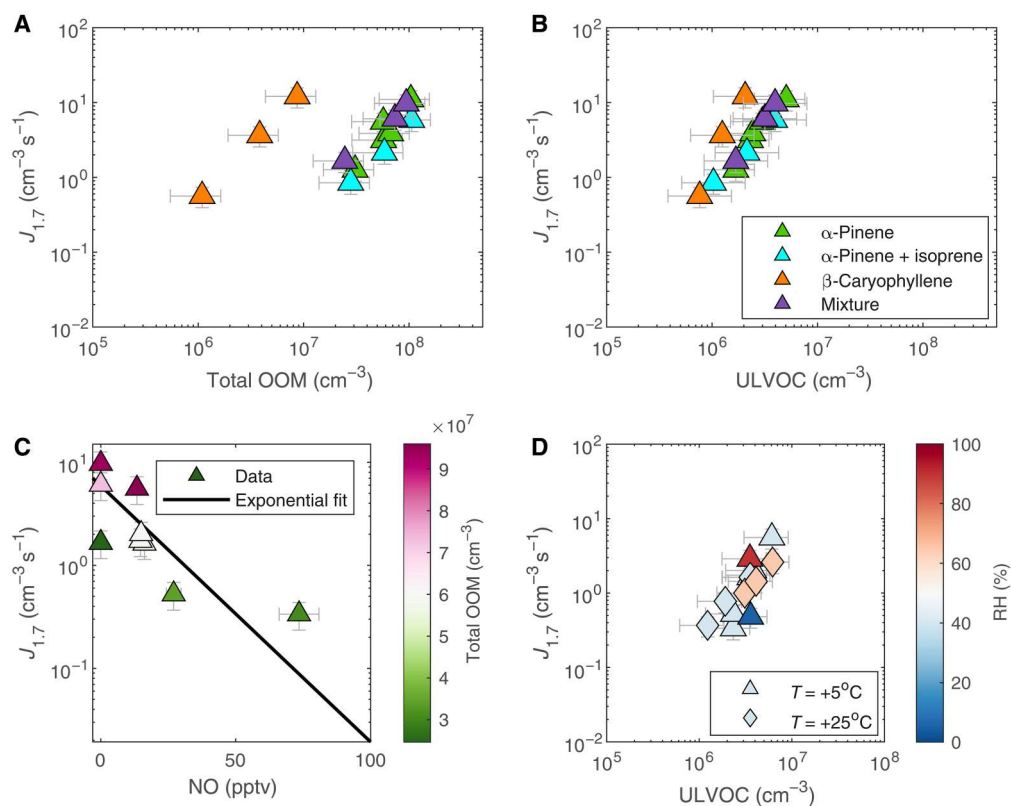
**Fig. 4. NPF rates versus vapor concentrations and different atmospheric conditions.** NPF rates at 1.7 nm ($J_{1.7}$) versus oxygenated vapor concentrations: (**A**) total OOM measured with NO$_3$-CIMS and (**B**) ULVOC measured with NO$_3$-CIMS. NPF rates are calculated for pure α-pinene (green), mixtures of α-pinene + isoprene (cyan), pure β-caryophyllene (orange), and mixtures of α-pinene + isoprene + β-caryophyllene (purple) at 5°C and 40% RH under galactic cosmic ray (GCR) conditions (see Materials and Methods) and 40 ppbv O$_3$. (**C**) Particle formation rates for α-pinene + isoprene + β-caryophyllene mixtures versus NO concentration at 5°C, 40% RH, 40 ppbv O$_3$, and GCR conditions. (**D**) Particle formation rates for α-pinene + isoprene + β-caryophyllene mixtures at 5° and 25°C versus ULVOC concentration measured with NO$_3$-CIMS, with the points colored according to RH. The experimental conditions are 40 ppbv O$_3$, 2- to 73-pptv NO, and GCR ionization.

molecules are needed to form a particle at 1.7 nm. It is also important to keep in mind that ULVOCs are not a single compound but a group of compounds of varying structures, functional groups, and a range of volatilities and likely do not behave the same during cluster formation processes. While the experimental conditions and NO concentrations affect the yield of the ULVOCs, once formed, these compounds contribute to particle formation with high efficiency (Fig. 6A). Particles from ULVOC nucleation form at atmospherically relevant rates observed in rural and mountain locations, where BVOCs are abundant (*42*). In particular, our results provide an explanation for the observed intense NPF events in the outflow of the Amazonian forest where a recent study estimates an ULVOC mixing ratio of around $3 \times 10^7$ cm$^{-3}$ (0.01 ppbv) between 0 and 5 km with even greater values at higher altitudes (*43*).

We find that the ULVOC concentration formed from a certain BVOC mixture (or single component) depends on the OOM production rate (from monoterpene and sesquiterpene), the sesquiterpene fraction in the mixture, and the availability of isoprene. Following expectations based on the ULVOC yields, pure β-caryophyllene produces the highest ULVOC concentrations per OOM production rate (from monoterpene and sesquiterpene), followed by pure α-pinene (Fig. 2B). The addition of isoprene in a 10:1 isoprene to monoterpene ratio reduces the ULVOC production by a factor of 1.5. However, the molar addition of only 1.8% β-

caryophyllene (few 100 pptv) is capable of restoring ULVOC levels close to pure α-pinene conditions (Fig. 2B), reversing the suppression effect by isoprene. The same applies to predicting the pure biogenic particle formation rate in which $J_{1.7}$ depends on the OOM production rate (from monoterpene and sesquiterpene), the sesquiterpene fraction in the mixture, and the availability of isoprene (Fig. 6B).

**Atmospheric implications**

We find that ULVOCs, with saturation concentrations, $C^*(T) \leq 3 \times 10^{-9}$ µg m$^{-3}$, are highly efficient nucleators, forming particles at 1% of the kinetic limit. Our measured particle formation rates at 1.7 nm, $J_{1.7}$, are determined by ULVOC concentrations alone, regardless of their origin, for all the mixtures of isoprene, monoterpene, and sesquiterpene reported here. The ULVOC yields per oxidation reaction are relatively small, below 1%, but they govern particle formation. The ULVOC class was proposed on the basis of expected saturation ratios to be the "nucleators," but their quantitative contribution to nucleation has not yet been quantified. Particle growth, in turn, is driven by more abundant but more volatile ELVOC and LVOC and tends to accelerate with particle size because of the Kelvin effect. Given the longer carbon backbone compared to α-pinene and isoprene, β-caryophyllene oxidation has higher ULVOC yields. Once they are formed, ULVOC nucleation occurs
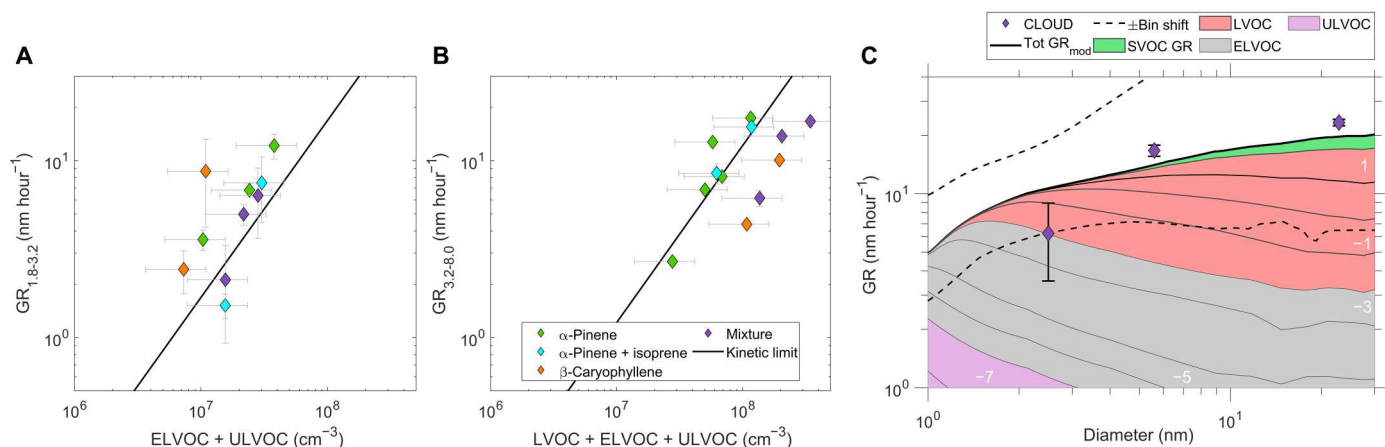
**Fig. 5. Growth rates versus vapor concentrations and particle diameter.** Particle growth rates during ozonolysis experiments for (**A**) particle diameters between 1.8 and 3.2 nm as a function of ELVOC + ULVOC concentrations measured with $NO_3$-CIMS and PTR3 and (**B**) particle diameters between 3.2 and 8 nm as a function of LVOC + ELVOC + ULVOC concentrations measured with $NO_3$-CIMS and PTR3. The black line shows the geometric limit of kinetic condensational growth for organics (300 Da and density of 1400 kg m$^{-3}$) (*41*). (**C**) Modeled and measured growth rates versus particle diameter for the three-component mixture experiment during ozonolysis at 5°C and 40% RH. The growth rates measured with the DMA-train (differential mobility analyzer train) are shown as diamonds. The error bars show the measurement uncertainty (see the "Particle formation and growth rates" section in Materials and Methods). The color code represents the different VBS bins at 278 K, and their contribution is illustrated by the shaded areas. The uncertainty range on the modeled growth rate calculation is shown as dashed lines, corresponding to a ±1 bin shift of the VBS, i.e., a factor of 10 and 0.1 change of volatility. The contour labels indicate the volatilities of the vapors contributing to particle growth at each size, where white numbers represent the logarithm of the saturation mass concentration (in μg m$^{-3}$) at 300 K.
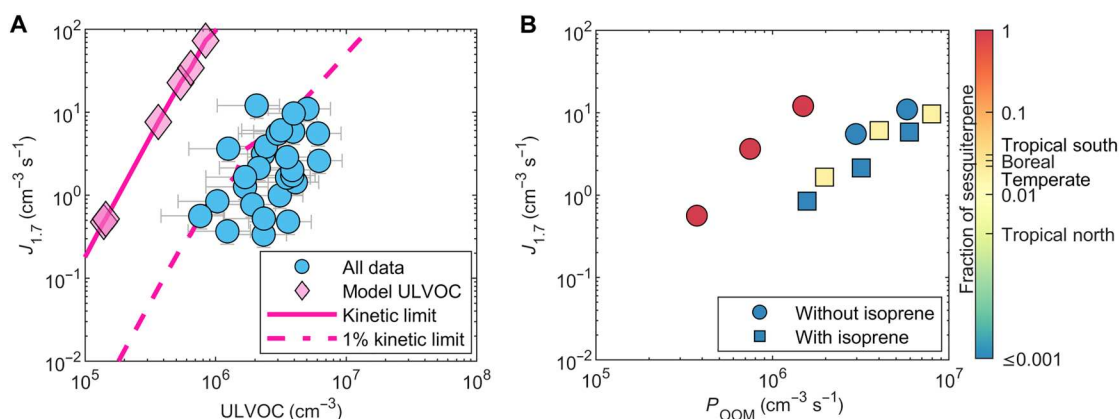


**Fig. 6. Pure biogenic nucleation relative to ULVOC kinetic limit.** (**A**) Particle formation rates at 1.7 nm ($J_{1.7}$) versus ULVOC measured with $NO_3$-CIMS for all data (blue circles; table S1), at $T$ = +5°C and +25°C and RH = 5 to 90% in the presence or absence of NO and any combination of α-pinene, β-caryophyllene, and isoprene. The formation rates derived from our kinetic model calculation for ULVOC nucleation are shown as diamonds, which are fitted by the magenta solid line (see the "Kinetic model for ULVOC nucleation" section in Materials and Methods); the dashed line simulates 1% kinetic limit (1% kinetic limit is calculated from dividing $J_{kinetic}$ by a factor 100). (**B**) Particle formation rates versus OOM production rate for different BVOC systems, where the points are colored according to the sesquiterpene molar fraction (injection concentrations). The experimental conditions are 5°C and RH = 40%. For comparison, Messina *et al.* (*13*) find in their emission budgets average sesquiterpene fractions of between 0.019 to 0.03 for boreal, temperate, and tropical southern regions and 0.003 for tropical northern regions shown in the color bar axis.

near the 1% kinetic limit, explaining the particle formation in locations (e.g., Amazonian outflow) where intense nucleation occurs but anthropogenic vapors are insufficient to explain the nucleation. This is in contrast to total OOMs from different BVOC and different atmospheric conditions, which do not explain the variability in particle formation rate; ULVOCs, once formed, nucleate at the same rate regardless of the initial BVOC or mixture introduced.

In the presence of multiple BVOCs, we observe OOM dimers formed via $RO_2$-$RO_2$ pathway including cross-dimer formation of $RO_2$ from different BVOC. OOMs with longer carbon backbones exceeding 20 carbons are formed from at least one β-caryophyllene

molecule. While the addition of isoprene to α-pinene reduces ULVOC yields by introducing $C_5$-$RO_2$, resulting in dimers with shorter carbon backbones, the molar addition of only 1.8% (few pptv) of β-caryophyllene to an α-pinene and isoprene mixture results in a twofold increase of ULVOC concentration per total oxidation products and, thus, an enhanced particle formation rate, reversing the "isoprene suppression" effect. Therefore, atmospheric particle formation rates from BVOC depend on the ULVOC concentration, which is dependent on the sesquiterpene fraction in the mixture.

Our observations could explain the intense nucleation events occurring above of tropical rainforests and in their outflows (43, 44), which cannot be explained by monoterpenes and isoprene alone. The results also show that, irrespective of their low mixing ratios in the atmosphere, sesquiterpenes may play a notable role in NPF and early growth. This has been overlooked and therefore globally underestimated. Therefore, we encourage the inclusion of sesquiterpenes in global models to better estimate the BVOC contribution to aerosol and CCN budgets in the past and future climate where biogenic emissions are expected to dominate or strongly contribute to NPF. Given the increased emissions of sesquiterpenes due to environmental stress that plants are subject to with the ongoing global temperature increase (7), understanding the contribution of sesquiterpenes to NPF and growth in the atmosphere is thus also important for a future affected by climate change. With future projected decreases in $SO_2$ emissions, pure biogenic nucleation is expected to play a more important role in the future. These results are equally important for understanding the pristine preindustrial era and present remote locations where biogenic emissions are dominant.

## MATERIALS AND METHODS
### The CLOUD experiment
The CLOUD chamber located at CERN, Geneva, Switzerland, is a 26.1-$m^3$ electropolished stainless-steel chamber with minimal contamination ideal for studying NPF at molecular level and at atmospherically relevant concentrations of precursors. The chamber is supplied with synthetic air from evaporated liquid nitrogen and oxygen. It can be supplied with around 25 trace gases at concentrations as low as 1 pptv from concentrated sources via a flexible ultra-clean gas system. Mixing inside the chamber is achieved by two fans at the top and bottom of the chamber. The chamber is equipped with a high-voltage mesh that, when turned on, removes all ions from the chamber, allowing for experiments under "neutral" conditions. Given the known role of ions in pure biogenic NPF (2), in this study, we focus on experiments with ions formed naturally in the chamber by galactic cosmic rays, referred to as "galactic cosmic ray" (GCR) runs. Runs at increased ion concentrations were performed using an adjustable π+ beam from the CERN Proton Synchrotron (45). The π+ beam is defocused to a transverse size of about 1.5 m by 1.5 m when it passes through the CLOUD chamber. With the electric field set to zero, the equilibrium total ion concentration (negative + positive ions) in the chamber due to GCRs is around 1500 $cm^{-3}$. With the π+ beam, this can be increased to any value up to about 6000 $cm^{-3}$. The chamber is equipped with state-of-the-art instrumentation measuring gas- and particle-phase concentration and chemical composition, described in detail in the next section.

### Instrumentation
#### Particle counters
The particle number size distribution in the size range between 1.2 nm and 1 μm was measured using a series of overlapping aerosol instruments. First, the size distribution of particles in the size range 1.2 to 3 nm was measured using a particle size magnifier [PSM; Airmodus Ltd. (46, 47)] operated in scanning mode connected in series to a condensational particle counter. The total concentration of particles with diameters equal or larger than 2.5 nm was measured using a butanol condensation particle counter (CPC

3776, TSI Inc.). The size distribution of particles between 1.8 and 8 nm was measured using a DMA-train (differential mobility analyzer train), which consists of six DMAs with a PSM or CPC as detector operating in parallel (48). In addition, the particle size distribution between 8 and 63 nm was measured using a commercial nanoscanning mobility particle sizer (nSMPS 3982, TSI Inc.). Last, larger particles with diameters larger than 50 nm were measured using a home-built long-SMPS system. The particle number size distribution data was averaged to 5 minutes time resolution. The negative and positive ion concentrations in the size range 0.8 to 45 nm were measured using a Neutral cluster and Air Ion Spectrometer [NAIS; Airel Ltd., Estonia (49)].

#### Nitrate ion chemical ionization mass spectrometer
Nucleating precursor gases and molecular clusters were measured by a NO$_3$-CIMS (50). The custom-built ion-source is based on the design by Eisele and Tanner (51) creating nitrate reagent ions $(HNO_3)_n NO_3^-$ with $n = 0$–2 by corona discharge, which are then focussed towards the sample flow. The resulting sample ions were analysed by a commercially available high-resolution atmospheric-pressure interface time of flight mass spectrometer (APi-TOF, Tofwerk AG, Thun, Switzerland). The nitrate ionization technique is highly selective towards sulfuric acid, iodic acid, dimethylamine and multifunctional OOMs. The instrument was calibrated for sulfuric acid according to Kürten et al. (52). Because of the lack of appropriate standards and the high reactivity of OOMs, a direct quantitative calibration of these compounds is not possible. However, as shown in previous studies (53), we can assume a detection efficiency of OOMs with an O:C ratio > 0.6 by the nitrate reagent ions similar to $H_2SO_4$, after correcting for the (measured) instrumental mass dependent transmission efficiency (54). Because of reduced presence of functional groups, such as hydroperoxy (−OOH) or hydroxy (−OH) groups, required for clustering with the nitrate reagent ion, OOMs with O:C ratio < 0.6 can be prone to a lower charging efficiency and an increased thermal dissociation of the ion-molecule cluster in the mass analyser (55). This leads to a lower detection efficiency of OOM with O:C ratio < 0.6 compared to sulfuric acid. In terms of quantity, the concentrations of these compounds can therefore only be regarded as lower limits.

#### Proton transfer reaction mass spectrometer–time of flight
Volume mixing ratios of precursors and oxidized products were monitored by the PTR3 TOF mass spectrometer (56) with limits of detection down to several hundred parts per quadrillion (ppqv). Protonated water clusters ($H_3O+(H_2O)_n$ with $n = 1...3$) act as reagent ions in a drift tube with controlled collision energy. This ensures fast ionization reactions with many OOMs close to the kinetic limit. Sensitivity to precursors was calibrated regularly by injecting known concentrations mixed from prepared gas standards and zero air for most precursors. As with the NO$_3$-CIMS, the sensitivity to product compounds has to be estimated based on precursor calibrations. Losses of low-volatility compounds due to collisions with inlet line walls were corrected similar to Stolzenburg et al. (32). PTR3 measurements cover VOC and SVOC (semivolatile organic compounds), and complement CIMS measurements for LVOC. The combination of these two instruments covers the mass range suitable for our study (57). Measurements using PTR3 are only available for the runs when no NO$_x$ was added (runs 1 to 14; table S1), and hence we rely on the NO$_3^-$CIMS for most of the runs' ULVOC estimation unless specified otherwise. See fig. S5 for

comparison between ULVOC from $NO_3^-$ CIMS and PTR3 and $NO_3^-$ CIMS combined.

### Filter inlet for gases and AEROsols

We measured the chemical composition of particle-phase OOMs and estimated their volatility via thermal desorption using an iodine-adduct CIMS equipped with a Filter Inlet for Gases and AEROsols ($I^-$ FIGAERO CIMS) (58). FIGAERO has two operation modes. In the "sampling" mode, gases are directly sampled into a 150 mbar ion-molecule reactor while particles are concurrently collected on a PTFE filter via a separate dedicated port. In the "desorption" mode, the filter is moved to another port where a pure $N_2$ gas stream is progressively heated before flowing through the filter to evaporate the particles via temperature-programmed desorption; the vaporized molecules are then introduced into the ion-molecule reactor and analysed by the CIMS. We estimated the volatility of all particle-phase OOMs based on the correlation between the vaporization enthalpy and the distinct maximum desorption temperature ($T_{max}$) of the thermograms during thermal desorption (59). The temperature–volatility calibration curve is established by correlating the measured $1/T_{max}$ ($K^{-1}$) with the sub-cooled liquid vapor pressure of a suite of standard carboxylic acids (60). It should be noted that thermal decomposition of a dimer into two monomers can occur during heating. This may lead to doublet-peaks in the thermogram (61) and is thus a potential source of uncertainty in volatility estimation.

### Trace gas monitors

The ozone ($O_3$) concentration was monitored using a Thermo Environmental Instruments TEI 49C. The sulphur dioxide ($SO_2$) concentration was monitored using a Thermo Fisher Scientific, Inc. 42i-TLE. Nitrogen monoxide (NO) was monitored using an ECO PHYSICS CLD 780 TR and nitrogen dioxide ($NO_2$) using a CE-DOAS, University of Colorado Boulder; and a CAPS, Aerodyne Research Inc.. The water vapor concentration in the chamber was measured using a chilled dew-point mirror (Edgetech Instruments) and a direct tuneable diode laser absorption spectrometer (similar as the APicT TDL hygrometer (62)). The in-chamber temperature was monitored using multiple thermocouples, while the wall temperature was measured using multiple Pt100 sensors (63).

### Data analysis

#### Definition of OOM

In this study, we consider all molecules that contain at least one carbon atom, one hydrogen atom, and one oxygen atom as OOMs.

#### Volatility bin calculation

Direct volatility measurements for all compounds found in the gas phase are not feasible because of low signals of many OOMs in the FIGAERO desorption profiles. Typically, parametrizations using the oxygen and carbon number inferred from mass spectrometric peak identification are applied to estimate the volatility of individual compounds. To evaluate the capability of these parametrizations to estimate the volatility of the OOMs from sesquiterpenes, we compared the measured volatility of $C_{15}$ compounds using an $I^-$ FIGAERO CIMS (using calibrated thermal desorption to directly determine the volatilities of individual components), the $C_{15}$ SIMPOL functional group–derived volatility using assumed molecular structures (fig. S3), and the $C_{15}$ composition-volatility relations adapted from the work of Stolzenburg et al. (32) for β-caryophyllene monomers ($C_{15}$) and mixed-phase dimers ($C_{5+10}$; table S2). The functional groups of β-caryophyllene oxygenated compounds

used for running the SIMPOL model (64) are given in fig. S3. The measured volatility is independent of the precursor identity and agrees well with the composition-volatility relations by the SIMPOL model (fig. S4). Our results show that monomer products from β-caryophyllene oxidation have very similar intrinsic volatility to (cross) dimer products from α-pinene + isoprene. Our results also validate using the parametrization adapted from the work of Stolzenburg et al. (32) to estimate the volatility of the different OOMs as long as the molecules with a carbon backbone up to 15 carbon atoms are treated as a monomer in the parametrization.

Because of the above confirmation of the parametrization of Stolzenburg et al. (32), we use Eq. 1A and Eq. 1B and the carbon ($n_C^i$), oxygen ($n_O^i$), and nitrogen ($n_N^i$) number identified by high-resolution mass spectrometry for all our volatility estimates. We adjusted the parametrization introduced by Stolzenburg et al. (32) for non-nitrated biogenic (CHO) to also incorporate nitrated systems (CHNO) as described by Stolzenburg et al. (65)

$$\log_{10} C_i^*(300\ K)[\mu g\ m^{-3}] = (n_C^0 - n_C^i) \times b_c - n_O^i \times b_{O,adj.}$$
$$- 2 \times \frac{n_C^i \times n_O^i}{n_C^i + n_O^i} \times b_{CO} \qquad (1A)$$

$$\log_{10} C_i^*(300\ K)[\mu g\ m^{-3}] = (n_C^0 - n_C^i) \times b_c - (n_O^i - 3n_N^i)$$
$$\times b_{O,adj.} - 2$$
$$\times \frac{n_C^i \times (n_O^i - 3n_N^i)}{n_C^i + (n_O^i - 3n_N^i)} \times b_{CO}$$
$$- b_N \times n_N^i \qquad (1B)$$

Apart from the well-characterized effect of on average half a decade in volatility per added carbon ($b_c = 0.475$), the reference volatility of 1 μg $m^{-3}$ for an alkene with 25 carbon atoms ($n_C^0 = 25$), and the nonlinearity term ($b_{CO} = -0.3$), the effect of oxygen on volatility depends on the abundance of different functionalization (64, 66). While using the "traditional" VBS, we find mostly equal ratios of alcohols, carbonyls, and carboxylic acids in multigeneration oxidation products with an average effect of $b_O = 2.3$ (60), the autoxidation of biogenic precursors also results in a substantial amount of hydroperoxides and hydroperoxyacids, which, on average, have a weaker effect on reducing the volatility per oxygen atom than the before-mentioned three groups (32, 64), resulting in a $b_{O,adj.} = 1.4$. However, covalently bound dimers most likely have a peroxide dimer bond with an even smaller effect on volatility per oxygen compared to the more polar carbonyls, carboxylic acids, and even hydroperoxides (67). Therefore, $b_{O,adj.} = 1.17$ is used for dimers ($n_C > 10$ for α-pinene and $n_C > 15$ for β-caryophyllene). This presents a challenge in the case of the mixture because molecules with $C_{11}$-$C_{15}$ cannot be unambiguously identified as monomers from β-caryophyllene autoxidation or dimers from covalently bound α-pinene and isoprene $RO_2$ radicals. Figure S4, however, shows, with direct volatility measurements using the FIGAERO-CIMS, that the $C_{15}$ products in the α-pinene+ β-caryophyllene +isoprene mixture follow closely the monomer volatility parametrization, which is therefore applied in the following for all α-pinene+ β-caryophyllene +isoprene experiments. Last, $b_N = 2.5$ and accounts for the three oxygen atoms within the nitrate group (68).

The parametrization of Eq. 1A is then used to classify each molecule into volatility bins, separated by one order of magnitude in saturation mass concentration $C_i^*$ at 300 K forming a so-called volatility basis set (VBS model) (66). As the experiments were performed at 5°C, the volatility distribution needs to be shifted, and the temperature-dependent volatility at temperature $T$ (in Kelvin) can be calculated using the Clausius-Clapeyron equation

$$\log_{10} C_i^*(T)[\mu g\ m^{-3}] = \log_{10} C_i^*(300\ K) + \frac{\Delta H_i^{\text{vap}}}{R\ln(10)}$$
$$\times \left(\frac{1}{300} - \frac{1}{T}\right) \quad (2)$$

where $\Delta H_i^{\text{vap}}$ is the evaporation enthalpy and can be approximated according to Stolzenburg et al. (32) as

$$\Delta H_i^{\text{vap}}[\text{kJ mol}^{-1}] = -5.7 \times \log_{10} C_i^*(300\ K) + 129 \quad (3)$$

A broad classification of volatility can be done as follows: SVOCs, $0.3\ \mu g\ m^{-3} < C^*(T) < 300\ \mu g\ m^{-3}$; LVOCs, $3 \times 10^{-5} < C^*(T) < 0.3\ \mu g\ m^{-3}$; ELVOCs, $3 \times 10^{-9} < C^*(T) < 3 \times 10^{-5}\ \mu g\ m^{-3}$; and ULVOCs, $C^*(T) \leq 3 \times 10^{-9}\ \mu g\ m^{-3}$. This volatility classification can be broadly translated into units of saturation number concentration assuming an average molecular weight of 300 Da, resulting in SVOCs ranging from $6 \times 10^8\ cm^{-3} < N_{eq} < 6 \times 10^{11}\ cm^{-3}$, LVOCs ranging from $6 \times 10^4\ cm^{-3} < N_{eq} < 6 \times 10^8\ cm^{-3}$, ELVOC ranging from $6 \times 10^0\ cm^{-3} < N_{eq} < 6 \times 10^4\ cm^{-3}$, and ULVOC including all substances with $N_{eq} \leq 6 \times 10^0\ cm^{-3}$, indicating that ULVOC compounds with abundances as low as a few tens per $cm^{-3}$ are eventually already in high gas-phase supersaturation, driving nucleation.

The VBS can subsequently be used to dynamically model the growth of a monodisperse aerosol population, indicative for the growth observed in our chamber experiments. More details can be found in the work of Stolzenburg et al. (65).

### OOM yields
The production rate of OOMs can be calculated from the injection and reaction rates as follows

$$\frac{d[\text{Precursor}]}{dt} = \frac{F}{V} \times [\text{Precursor}]_0 - k_{O_3} \times [O_3] \times [\text{Precursor}]_t$$
$$- k_{OH} \times [OH] \times [\text{Precursor}]_t - \frac{F}{V}$$
$$\times [\text{Precursor}]_t \quad (4)$$

Here, $F$ is the flow rate inside the CLOUD chamber, here constant at 0.225 $m^3\ min^{-1}$, and $V$ is the volume of the CLOUD chamber (26.1 $m^3$). Thus, $\frac{F}{V}$ represents the dilution rate in the chamber during these runs, which is ~0.5 $hour^{-1}$. The injected and measured concentrations of a precursor (α-pinene, β-caryophyllene, or isoprene) are represented as $[\text{Precursor}]_0$ and $[\text{Precursor}]_t$, respectively.

Let the production of OOM ($P_{OOM}$) be

$$P_{OOM} = k_{O_3} \times [O_3] \times [\text{Precursor}]_t + k_{OH} \times [OH]$$
$$\times [\text{Precursor}]_t \quad (5)$$

At steady state, we obtain

$$\frac{d[\text{Precursor}]}{dt} = 0$$
$$= \frac{F}{V} \times [\text{Precursor}]_0 - P_{OOM} - \frac{F}{V} \times [\text{Precursor}]_t \quad (6)$$

which can be rearranged as

$$P_{OOM} = \frac{F}{V} \times [\text{Precursor}]_0 - \frac{F}{V} \times [\text{Precursor}]_t \quad (7)$$

The production of ULVOCs can then be written as

$$\frac{d[\text{ULVOC}]}{dt} = \gamma_{\text{ULVOC}} \times P_{OOM} - k_{\text{wall}} \times [\text{ULVOC}] - CS$$
$$\times [\text{ULVOC}] - \frac{F}{V} \times [\text{ULVOC}] \quad (8)$$

where $\gamma_{\text{ULVOC}}$ is the yield of ULVOC, $k_{\text{wall}}$ is the wall loss rate, and CS is the condensation sink.

At steady state, the yield of ULVOC ($\gamma_{\text{ULVOC}}$) can be calculated as follows

$$\gamma_{\text{ULVOC}} = \frac{\left\{\left(k_{\text{wall}} + CS + \frac{F}{V}\right) \times [\text{ULVOC}]\right\}}{P_{OOM}} \quad (9)$$

### Particle formation and growth rates
The particle formation rates were calculated at the cutoff diameter 1.7 nm via the balance equation described by Dada et al. (69) in which the formation rate ($J_{1.7}$) is determined from the time derivative of the total concentration of particles with diameters larger or equal to 1.7 nm and accounting for the particle dilution ($S_{\text{dil}}$), coagulation ($S_{\text{coag}}$), and wall ($S_{\text{wall}}$) losses in the chamber (2, 69)

$$J_{1.7}[\text{cm}^{-3}\ \text{s}^{-1}] = \frac{dN_{>1.7\ nm}}{dt} + S_{\text{dil}} + S_{\text{coag}} + S_{\text{wall}} \quad (10)$$

$N_{>1.7}$ is the total concentration of particles with diameters equal to or larger than 1.7 nm measured and integrated using multiple particle counters.

The dilution loss rate is

$$S_{\text{dil}}[\text{cm}^{-3}\ \text{s}^{-1}] = N_{>1.7\ nm} \cdot k_{\text{dil}} \quad (11)$$

with

$$k_{\text{dil}}[\text{s}^{-1}] = \frac{\text{Flow}_{\text{synthetic air}}}{V_{\text{chamber}}} \quad (12)$$

where $k_{\text{dil}}$ is the dilution rate, $\text{Flow}_{\text{synthetic air}}$ is the flow rate of clean air, here, 0.225 $m^3\ min^{-1}$, and $V_{\text{chamber}}$ is the volume of the chamber, 26.1 $m^3$.

The size distribution–dependent coagulation loss rate

$$S_{\text{coag}}(1.7\ \text{nm})[\text{cm}^{-3}\ \text{s}^{-1}] = \int K(d_p, d_p') n(d_p') dd_p'$$
$$\cong \sum_{d_p'=d_p}^{d_p'=\text{max}} K(d_p, d_p') N_{d_p'}\ [\text{cm}^{-3}\ \text{s}^{-1}] \quad (13)$$

where $K(d_p, d_p')$ is the Brownian coagulation coefficient for particle sizes $d_p$ and $d_p'$ (70).

The wall loss rate is

$$S_{\text{wall}} \; [\text{cm}^{-3} \; \text{s}^{-1}] = \sum_i N_{dpi-dpi+1} \cdot k_{\text{wall}} \quad (14)$$

where $dp_i$-$dp_{i+1}$ refers to the size-dependent number concentration, and $k_{\text{wall}}$ in units of $\text{s}^{-1}$ is determined experimentally for the CLOUD chamber at different temperatures using the diffusion of sulfuric acid monomers (diameter, ~0.82 nm) to the chamber wall. Under most circumstances, the experiments approach steady state and $J_{1.7} \sim = S_{\text{wall}}$. Uncertainty on particle formation rates from systematic and statistical errors is approximated to be 30% based on repeatability of measurements in the CLOUD chamber [see also the work of Dada *et al.* (*69*)].

The particle growth rates were determined using the 50% appearance time method (*69*) in which we determined the 50% appearance time by a sigmoidal fit to the time evolution of the signal at a specific diameter $d_p$ and obtained the growth rate by a linear orthogonal distance regression to the appearance time diameter curve for serval channels using different size range method (*69*). The uncertainty is calculated from the uncertainties of the linear regression, which includes the fitting uncertainties in the determination of the individual appearance times. Systematic effects such as coagulation or wall losses on the growth rate are neglected because of their minor influence at typical CLOUD conditions [see also the work of Ozon *et al.* (*71*)].

Particle growth was modeled using a monodisperse organic growth model as described by Stolzenburg *et al.* (*65*), which solves the set of coupled ordinary differential equations of mass transfer for each VBS bin

$$\frac{dc_{i,p}}{dt} = N_p k_{i,p} \left[ c_{i,g} - \frac{c_{i,p}}{\sum_i C_{i,p}} \exp\left( \frac{4\sigma_{OA} M_i}{RT\rho_{OA} d_p} \right) c_i^0 \right] \quad (15)$$

where $c_{i,p}$ is the mass concentration of each VBS-bin $i$ in the particle phase, $c_{i,g}$ is the mass concentration of each VBS-bin $i$ in the gas phase, and $c_i^0$ is the saturation mass concentration of the bin at the temperature of the experiment. $N_p$ is the monodisperse particle population number concentration, which does not influence the resulting growth rates of the model; $k_{i,p}$ is the collision rate coefficient for collision of a molecule of VBS-bin $i$ with the growing particle population (assumed to follow a hard-sphere collision kernel based on bulk density and spherical assumptions). The driving force of condensation is the difference between the gas-phase mass concentration created by the continuous oxidation of the organic precursors and the saturation mass concentration. The latter is modified by the Kelvin term to account for the curvature effect and the Raoult term, which accounts for the solution effect of the different VBS-bins into each other. This ultimately couples the differential equations for the different bins, requiring a numerical solution. Particle-phase activity coefficients are assumed to be unity in this study.

### Kinetic model for ULVOC nucleation
A kinetic model based on the general dynamic equation (*70*) was used to assess ULVOC nucleation; see the works of Xiao *et al.* (*72*) and Marten *et al.* (*73*) for the acid-base model version. The model considers neutral clusters containing up to 15 molecules and then 50 geometric size bins between clusters containing 16 ULVOC molecules and 1000 nm and uses a constant production rate (fig. S9). Note that a particle with a diameter of diameter

contained three ULVOC molecules. The model was run at 12 initial ULVOC production rates between 100 and $10^8 \text{ cm}^3 \text{ s}^{-1}$. All evaporation rates are set to zero for kinetic nucleation. A density of $1.2 \text{ g cm}^{-3}$ was used in the calculations.

The change in concentration of clusters containing 1 to 15 ULVOC molecules ($i$ = 1 to 15, $j$ = 1 to 15) is defined as follows

$$\frac{dN_i}{dt} = \frac{1}{2} \sum_{j=1}^{i-1} K_{j,i-j} N_j \; N_{i-j} - N_i \left( k_{\text{dil}} + k_{\text{wall},i} + \sum_{j=1}^{\infty} K_{i,j} N_j \right) \quad (16)$$

Then, 150 geometric sized bins are applied with collision of the particles distributed between the two nearest bins to allow for continuous growth

$$\frac{dN_i}{dt} = \frac{1}{2} \sum_{j+k \to i} K_{j,k} N_j \; N_k P_{j,k} + \frac{1}{2} \sum_{j+k \to i-1} K_{j,k} N_j \; N_k (1 - P_{j,k})$$
$$- N_i \left( k_{\text{dil}} + k_{\text{wall},i} + \sum_{j=1}^{\infty} K_{i,j} N_j \right) \quad (17)$$

The collision rates are calculated as

$$K_{i,j} = \left( \frac{3}{4\pi} \right)^{\frac{1}{6}} \left( \frac{6k_B T}{m_i} + \frac{6k_B T}{m_j} \right)^{\frac{1}{2}} (V_i^{\frac{1}{3}} + V_j^{\frac{1}{3}})^2 \quad (18)$$

$$P_{j,k} = \frac{V_{i+1} - V_j - V_k}{V_{i+1} - V_i} \quad (19)$$

where $V_i < V_j + V_k < V_{i+1}$.

The wall loss is calculated as

$$k_{\text{wall}} = C\sqrt{D} \quad (20)$$

$C$ is a chamber specific constant and depends on chamber dimensions and air mixing (fan speed). $C = 0.77 \text{ cm}^{-1} \text{ s}^{-0.5}$ is used in this study based on $0.002\text{-s}^{-1}$ sulfuric acid wall loss rate. $D$ is the diffusion constant calculated as

$$D = \frac{kTC_c}{3\pi\eta D_p} \quad (21)$$

where $k$, $T$, $C_C$, $\eta$, and $D_p$ are the Boltzmann constant, the temperature, the Cunningham slip correction factor, the gas viscosity, and the particle diameter, respectively.

## Supplementary Materials
**This PDF file includes:**
Figs. S1 to S9
Tables S1 and S2
References

## REFERENCES AND NOTES
1. A. B. Guenther, X. Jiang, C. L. Heald, T. Sakulyanontvittaya, T. Duhl, L. K. Emmons, X. Wang, The Model of Emissions of Gases and Aerosols from Nature version 2.1 (MEGAN2.1): An extended and updated framework for modeling biogenic emissions. *Geosci. Model Dev.* **5**, 1471–1492 (2012).
2. J. Kirkby, J. Duplissy, K. Sengupta, C. Frege, H. Gordon, C. Williamson, M. Heinritzi, M. Simon, C. Yan, J. Almeida, J. Tröstl, T. Nieminen, I. K. Ortega, R. Wagner, A. Adamov, A. Amorim, A. K. Bernhammer, F. Bianchi, M. Breitenlechner, S. Brilke, X. Chen, J. Craven, A. Dias, S. Ehrhart,

R. C. Flagan, A. Franchin, C. Fuchs, R. Guida, J. Hakala, C. R. Hoyle, T. Jokinen, H. Junninen, J. Kangasluoma, J. Kim, M. Krapf, A. Kürten, A. Laaksonen, K. Lehtipalo, V. Makhmutov, S. Mathot, U. Molteni, A. Onnela, O. Peräkylä, F. Piel, T. Petäjä, A. P. Praplan, K. Pringle, A. Rap, N. A. D. Richards, I. Riipinen, M. P. Rissanen, L. Rondo, N. Sarnela, S. Schobesberger, C. E. Scott, J. H. Seinfeld, M. Sipilä, G. Steiner, Y. Stozhkov, F. Stratmann, A. Tomé, A. Virtanen, A. L. Vogel, A. C. Wagner, P. E. Wagner, E. Weingartner, D. Wimmer, P. M. Winkler, P. Ye, X. Zhang, A. Hansel, J. Dommen, N. M. Donahue, D. R. Worsnop, U. Baltensperger, M. Kulmala, K. S. Carslaw, J. Curtius, Ion-induced nucleation of pure biogenic particles. *Nature* **533**, 521–526 (2016).

3. F. Bianchi, H. Junninen, A. Bigi, V. A. Sinclair, L. Dada, C. R. Hoyle, Q. Zha, L. Yao, L. R. Ahonen, P. Bonasoni, S. Buenrostro Mazon, P. Laj, K. Lehtipalo, J. Kangasluoma, V. M. Kerminen, J. Kontkanen, A. Marinoni, S. Mirme, U. Molteni, T. Petäjä, M. Riva, C. Rose, K. Sellegri, C. Yan, D. R. Worsnop, M. Kulmala, U. Baltensperger, J. Dommen, Biogenic particles formed in the Himalaya as an important source of free tropospheric aerosols. *Nat. Geosci.* **14**, 4–9 (2021).

4. K. R. Daellenbach, G. Uzu, J. Jiang, L. E. Cassagnes, Z. Leni, A. Vlachou, G. Stefenelli, F. Canonaco, S. Weber, A. Segers, J. J. P. Kuenen, M. Schaap, O. Favez, A. Albinet, S. Aksoyoglu, J. Dommen, U. Baltensperger, M. Geiser, I. el Haddad, J. L. Jaffrezo, A. S. H. Prévôt, Sources of particulate-matter air pollution and its oxidative potential in Europe. *Nature* **587**, 414–419 (2020).

5. S. Aksoyoglu, J. Jiang, G. Ciarelli, U. Baltensperger, A. S. H. Prévôt, Role of ammonia in European air quality with changing land and ship emissions between 1990 and 2030. *Atmos. Chem. Phys.* **20**, 15665–15680 (2020).

6. D. P. van Vuuren, J. Edmonds, M. Kainuma, K. Riahi, A. Thomson, K. Hibbard, G. C. Hurtt, T. Kram, V. Krey, J. F. Lamarque, T. Masui, M. Meinshausen, N. Nakicenovic, S. J. Smith, S. K. Rose, The representative concentration pathways: An overview. *Clim. Change* **109**, 5–31 (2011).

7. D. F. Zhao, A. Buchholz, R. Tillmann, E. Kleist, C. Wu, F. Rubach, A. Kiendler-Scharr, Y. Rudich, J. Wildt, T. F. Mentel, Environmental conditions regulate the impact of plants on cloud formation. *Nat. Commun.* **8**, 14067 (2017).

8. C. Faiola, D. Taipale, Impact of insect herbivory on plant stress volatile emissions from trees: A synthesis of quantitative measurements and recommendations for future research. *Atmospheric Environ. X* **5**, 100060 (2020).

9. H. Hellén, A. P. Praplan, T. Tykkä, A. Helin, S. Schallhart, P. P. Schiestl-Aalto, J. Bäck, H. Hakola, Sesquiterpenes and oxygenated sesquiterpenes dominate the VOC (C5–C20) emissions of downy birches. *Atmos. Chem. Phys.* **21**, 8045–8066 (2021).

10. T. R. Duhl, D. Helmig, A. Guenther, Sesquiterpene emissions from vegetation: A review. *Biogeosciences* **5**, 761–777 (2008).

11. L. Gao, J. Song, C. Mohr, W. Huang, M. Vallon, F. Jiang, T. Leisner, H. Saathoff, Kinetics, SOA yields, and chemical composition of secondary organic aerosol from β-caryophyllene ozonolysis with and without nitrogen oxides between 213 and 313 K. *Atmos. Chem. Phys.* **22**, 6001–6020 (2022).

12. J. P. Greenberg, A. B. Guenther, G. Pétron, C. Wiedinmyer, O. Vega, L. V. Gatti, J. Tota, G. Fisch, Biogenic VOC emissions from forested Amazonian landscapes. *Glob. Chang. Biol.* **10**, 651–662 (2004).

13. P. Messina, J. Lathière, K. Sindelarova, N. Vuichard, C. Granier, J. Ghattas, A. Cozic, D. A. Hauglustaine, Global biogenic volatile organic compound emissions in the ORCHIDEE and MEGAN models and sensitivity to key parameters. *Atmos. Chem. Phys.* **16**, 14169–14202 (2016).

14. K. Jardine, A. Yañez Serrano, A. Arneth, L. Abrell, A. Jardine, J. van Haren, P. Artaxo, L. V. Rizzo, F. Y. Ishida, T. Karl, J. Kesselmeier, S. Saleska, T. Huxman, Within-canopy sesquiterpene ozonolysis in Amazonia. *J. Geophys. Res. Atmos.* **116**, 10.1029/2011JD016243, (2011).

15. E. Bourtsoukidis, T. Behrendt, A. M. Yañez-Serrano, H. Hellén, E. Diamantopoulos, E. Catão, K. Ashworth, A. Pozzer, C. A. Quesada, D. L. Martins, M. Sá, A. Araujo, J. Brito, P. Artaxo, J. Kesselmeier, J. Lelieveld, J. Williams, Strong sesquiterpene emissions from Amazonian soils. *Nat. Commun.* **9**, 2226 (2018).

16. L. M. F. Barreira, A. Ylisirniö, I. Pullinen, A. Buchholz, Z. Li, H. Lipp, H. Junninen, U. Hõrrak, S. M. Noe, A. Krasnova, D. Krasnov, K. Kask, E. Talts, Ü. Niinemets, J. Ruiz-Jimenez, S. Schobesberger, The importance of sesquiterpene oxidation products for secondary organic aerosol formation in a springtime hemiboreal forest. *Atmos. Chem. Phys.* **21**, 11781–11800 (2021).

17. T. Sakulyanontvittaya, A. Guenther, D. Helmig, J. Milford, C. Wiedinmyer, Secondary organic aerosol from sesquiterpene and monoterpene emissions in the United States. *Environ. Sci. Technol.* **42**, 8784–8790 (2008).

18. L. D. Yee, G. Isaacman-VanWertz, R. A. Wernis, M. Meng, V. Rivera, N. M. Kreisberg, S. V. Hering, M. S. Bering, M. Glasius, M. A. Upshur, A. Gray Bé, R. J. Thomson, F. M. Geiger, J. H. Offenberg, M. Lewandowski, I. Kourtchev, M. Kalberer, S. de Sá, S. T. Martin, M. L. Alexander, B. B. Palm, W. Hu, P. Campuzano-Jost, D. A. Day, J. L. Jimenez, Y. Liu, K. A. McKinney, P. Artaxo, J. Viegas, A. Manzi, M. B. Oliveira, R. de Souza, L. A. T. Machado, K. Longo, A. H.

19. H. Junninen, L. Ahonen, F. Bianchi, L. Quéléver, S. Schallhart, L. Dada, H. E. Manninen, K. Leino, J. Lampilahti, S. Buenrostro Mazon, P. Rantala, M. Räty, J. Kontkanen, S. Negri, D. Aliaga, O. Garmash, P. Alekseychik, H. Lipp, K. Tamme, J. Levula, M. Sipilä, M. Ehn, D. Worsnop, S. Zilitinkevich, I. Mammarella, J. Rinne, T. Vesala, T. Petäjä, V. M. Kerminen, M. Kulmala, Terpene emissions from boreal wetlands can initiate stronger atmospheric new particle formation than boreal forests. *Commun. Earth Environ.* **3**, 93 (2022).

20. M. Boy, T. Karl, A. Turnipseed, R. L. Mauldin, E. Kosciuch, J. Greenberg, J. Rathbone, J. Smith, A. Held, K. Barsanti, B. Wehner, S. Bauer, A. Wiedensohler, B. Bonn, M. Kulmala, A. Guenther, New particle formation in the front range of the colorado rocky mountains. *Atmos. Chem. Phys.* **8**, 1577–1590 (2008).

21. B. Bonn, G. K. Moortgat, Sesquiterpene ozonolysis: Origin of atmospheric new particle formation from biogenic hydrocarbons. *Geophys. Res. Lett.* **30**, 10.1029/2003GL017000, (2003).

22. B. Bonn, A. Hirsikko, H. Hakola, T. Kurtén, L. Laakso, M. Boy, M. Dal Maso, J. M. Mäkelä, M. Kulmala, Ambient sesquiterpene concentration and its link to air ion measurements. *Atmos. Chem. Phys.* **7**, 2893–2916 (2007).

23. A. L. Vogel, J. Schneider, C. Müller-Tautges, T. Klimach, T. Hoffmann, Aerosol chemistry resolved by mass spectrometry: Insights into particle growth after ambient new particle formation. *Environ. Sci. Technol.* **50**, 10814–10822 (2016).

24. L. Pichelstorfer, D. Stolzenburg, J. Ortega, T. Karl, H. Kokkola, A. Laakso, K. E. J. Lehtinen, J. N. Smith, P. H. McMurry, P. M. Winkler, Resolving nanoparticle growth mechanisms from size- and time-dependent growth rate analysis. *Atmos. Chem. Phys.* **18**, 1307–1323 (2018).

25. M. Heinritzi, L. Dada, M. Simon, D. Stolzenburg, A. C. Wagner, L. Fischer, L. R. Ahonen, S. Amanatidis, R. Baalbaki, A. Baccarini, P. S. Bauer, B. Baumgartner, F. Bianchi, S. Brilke, D. Chen, R. Chiu, A. Dias, J. Dommen, J. Duplissy, H. Finkenzeller, C. Frege, C. Fuchs, O. Garmash, H. Gordon, M. Granzin, I. el Haddad, X. He, J. Helm, V. Hofbauer, C. R. Hoyle, J. Kangasluoma, T. Keber, C. Kim, A. Kürten, H. Lamkaddam, T. M. Laurila, J. Lampilahti, C. P. Lee, K. Lehtipalo, M. Leiminger, H. Mai, V. Makhmutov, H. E. Manninen, R. Marten, S. Mathot, R. L. Mauldin, B. Mentler, U. Molteni, T. Müller, W. Nie, T. Nieminen, A. Onnela, E. Partoll, M. Passananti, T. Petäjä, J. Pfeifer, V. Pospisilova, L. L. J. Quéléver, M. P. Rissanen, C. Rose, S. Schobesberger, W. Scholz, K. Scholze, M. Sipilä, G. Steiner, Y. Stozhkov, C. Tauber, Y. J. Tham, M. Vazquez-Pufleau, A. Virtanen, A. L. Vogel, R. Volkamer, R. Wagner, M. Wang, L. Weitz, D. Wimmer, M. Xiao, C. Yan, P. Ye, Q. Zha, X. Zhou, A. Amorim, U. Baltensperger, A. Hansel, M. Kulmala, A. Tomé, P. M. Winkler, D. R. Worsnop, N. M. Donahue, J. Kirkby, J. Curtius, Molecular understanding of the suppression of new-particle formation by isoprene. *Atmos. Chem. Phys.* **20**, 11809–11821 (2020).

26. F. Bianchi, T. Kurtén, M. Riva, C. Mohr, M. P. Rissanen, P. Roldin, T. Berndt, J. D. Crounse, P. O. Wennberg, T. F. Mentel, J. Wildt, H. Junninen, T. Jokinen, M. Kulmala, D. R. Worsnop, J. A. Thornton, N. Donahue, H. G. Kjaergaard, M. Ehn, Highly oxygenated organic molecules (HOM) from gas-phase autoxidation involving peroxy radicals: A key contributor to atmospheric aerosol. *Chem. Rev.* **119**, 3472–3509 (2019).

27. J. D. Crounse, L. B. Nielsen, S. Jørgensen, H. G. Kjaergaard, P. O. Wennberg, Autoxidation of organic compounds in the atmosphere. *J. Phys. Chem. Lett.* **4**, 3513–3520 (2013).

28. G. McFiggans, T. F. Mentel, J. Wildt, I. Pullinen, S. Kang, E. Kleist, S. Schmitt, M. Springer, R. Tillmann, C. Wu, D. Zhao, M. Hallquist, C. Faxon, M. le Breton, A. M. Hallquist, D. Simpson, R. Bergström, M. E. Jenkin, M. Ehn, J. A. Thornton, M. R. Alfarra, T. J. Bannan, C. J. Percival, M. Priestley, D. Topping, A. Kiendler-Scharr, Secondary organic aerosol reduced by mixture of atmospheric vapours. *Nature* **565**, 587–593 (2019).

29. J. Tröstl, W. K. Chuang, H. Gordon, M. Heinritzi, C. Yan, U. Molteni, L. Ahlm, C. Frege, F. Bianchi, R. Wagner, M. Simon, K. Lehtipalo, C. Williamson, J. S. Craven, J. Duplissy, A. Adamov, J. Almeida, A. K. Bernhammer, M. Breitenlechner, S. Brilke, A. Dias, S. Ehrhart, R. C. Flagan, A. Franchin, C. Fuchs, R. Guida, M. Gysel, A. Hansel, C. R. Hoyle, T. Jokinen, H. Junninen, J. Kangasluoma, H. Keskinen, J. Kim, M. Krapf, A. Kürten, A. Laaksonen, M. Lawler, M. Leiminger, S. Mathot, O. Möhler, T. Nieminen, A. Onnela, T. Petäjä, F. M. Piel, P. Miettinen, M. P. Rissanen, L. Rondo, N. Sarnela, S. Schobesberger, K. Sengupta, M. Sipilä, J. N. Smith, G. Steiner, A. Tomè, A. Virtanen, A. C. Wagner, E. Weingartner, D. Wimmer, P. M. Winkler, P. Ye, K. S. Carslaw, J. Curtius, J. Dommen, J. Kirkby, M. Kulmala, I. Riipinen, D. R. Worsnop, N. M. Donahue, U. Baltensperger, The role of low-volatility organic compounds in initial particle growth in the atmosphere. *Nature* **533**, 527–531 (2016).

30. M. Simon, L. Dada, M. Heinritzi, W. Scholz, D. Stolzenburg, L. Fischer, A. C. Wagner, A. Kürten, B. Rörup, X. C. He, J. Almeida, R. Baalbaki, A. Baccarini, P. S. Bauer, L. Beck, A. Bergen, F. Bianchi, S. Bräkling, S. Brilke, L. Caudillo, D. Chen, B. Chu, A. Dias, D. C. Draper, J. Duplissy, I. el-Haddad, H. Finkenzeller, C. Frege, L. Gonzalez-Carracedo, H. Gordon, M. Granzin, J. Hakala, V. Hofbauer, C. R. Hoyle, C. Kim, W. Kong, H. Lamkaddam, C. P. Lee, K. Lehtipalo, M. Leiminger, H. Mai, H. E. Manninen, G. Marie, R. Marten, B. Mentler, U. Molteni, L. Nichman, W. Nie, A. Ojdanic, A. Onnela, E. Partoll, T. Petäjä, J. Pfeifer, M. Philippov, L. L. J. Quéléver, A. Ranjithkumar, M. P. Rissanen, S. Schallhart, S. Schobesberger, S. Schuchmann, J. Shen, M. Sipilä, G. Steiner, Y. Stozhkov, C. Tauber, Y. J. Tham, A. R. Tomé, M. Vazquez-Pufleau, A. L.

Vogel, R. Wagner, M. Wang, D. S. Wang, Y. Wang, S. K. Weber, Y. Wu, M. Xiao, C. Yan, P. Ye, Q. Ye, M. Zauner-Wieczorek, X. Zhou, U. Baltensperger, R. C. Flagan, A. Hansel, M. Kulmala, R. Volkamer, P. M. Winkler, D. R. Worsnop, N. M. Donahue, J. Kirkby, J. Curtius, Molecular understanding of new-particle formation from α-pinene between −50 and +25°C. *Atmos. Chem. Phys.* **20**, 9183–9207 (2020).

31. S. Richters, H. Herrmann, T. Berndt, Highly oxidized $RO_2$ radicals and consecutive products from the ozonolysis of three sesquiterpenes. *Environ. Sci. Technol.* **50**, 2354–2362 (2016).

32. D. Stolzenburg, L. Fischer, A. L. Vogel, M. Heinritzi, M. Schervish, M. Simon, A. C. Wagner, L. Dada, L. R. Ahonen, A. Amorim, A. Baccarini, P. S. Bauer, B. Baumgartner, A. Bergen, F. Bianchi, M. Breitenlechner, S. Brilke, S. Buenrostro Mazon, D. Chen, A. Dias, D. C. Draper, J. Duplissy, I. el Haddad, C. Frege, C. Fuchs, O. Garmash, H. Gordon, X. He, J. Helm, V. Hofbauer, C. R. Hoyle, C. Kim, J. Kirkby, J. Kontkanen, A. Kürten, M. Lawler, K. Lehtipalo, M. Leiminger, H. Mai, S. Mathot, B. Mentler, U. Molteni, W. Nie, T. Nieminen, J. B. Nowak, A. Ojdanic, A. Onnela, M. Passananti, T. Petäjä, L. L. J. Quéléver, M. P. Rissanen, N. Sarnela, S. Schallhart, C. Tauber, A. Tomé, R. Wagner, M. Wang, L. Weitz, D. Wimmer, M. Xiao, C. Yan, P. Ye, Q. Zha, U. Baltensperger, J. Curtius, J. Dommen, R. C. Flagan, M. Kulmala, J. N. Smith, D. R. Worsnop, A. Hansel, N. M. Donahue, P. M. Winkler, Rapid growth of organic aerosol nanoparticles over a wide tropospheric temperature range. *Proc. Natl. Acad. Sci. U.S.A.* **115**, 9122–9127 (2018).

33. U. Molteni, M. Simon, M. Heinritzi, C. R. Hoyle, A. K. Bernhammer, F. Bianchi, M. Breitenlechner, S. Brilke, A. Dias, J. Duplissy, C. Frege, H. Gordon, C. Heyn, T. Jokinen, A. Kürten, K. Lehtipalo, V. Makhmutov, T. Petäjä, S. M. Pieber, A. P. Praplan, S. Schobesberger, G. Steiner, Y. Stozhkov, A. Tomé, J. Tröstl, A. C. Wagner, R. Wagner, C. Williamson, C. Yan, U. Baltensperger, J. Curtius, N. M. Donahue, A. Hansel, J. Kirkby, M. Kulmala, D. R. Worsnop, J. Dommen, Formation of highly oxygenated organic molecules from α-pinene ozonolysis: Chemical characteristics, mechanism, and kinetic model development. *ACS Earth Space Chem.* **3**, 873–883 (2019).

34. Y. Luo, O. Garmash, H. Li, F. Graeffe, A. P. Praplan, A. Liikanen, Y. Zhang, M. Meder, O. Peräkylä, J. Peñuelas, A. M. Yáñez-Serrano, M. Ehn, Oxidation product characterization from ozonolysis of the diterpene ent-kaurene. *Atmos. Chem. Phys.* **22**, 5619–5637 (2022).

35. M. Schervish, N. M. Donahue, Peroxy radical chemistry and the volatility basis set. *Atmos. Chem. Phys.* **20**, 1183–1199 (2020).

36. C. Yan, W. Nie, A. L. Vogel, L. Dada, K. Lehtipalo, D. Stolzenburg, R. Wagner, M. P. Rissanen, M. Xiao, L. Ahonen, L. Fischer, C. Rose, F. Bianchi, H. Gordon, M. Simon, M. Heinritzi, O. Garmash, P. Roldin, A. Dias, P. Ye, V. Hofbauer, A. Amorim, P. S. Bauer, A. Bergen, A.-K. Bernhammer, M. Breitenlechner, S. Brilke, A. Buchholz, S. B. Mazon, M. R. Canagaratna, X. Chen, A. Ding, J. Dommen, D. C. Draper, J. Duplissy, C. Frege, C. Heyn, R. Guida, J. Hakala, L. Heikkinen, C. R. Hoyle, T. Jokinen, J. Kangasluoma, J. Kirkby, J. Kontkanen, A. Kürten, M. J. Lawler, H. Mai, S. Mathot, R. L. Mauldin, U. M. III, L. Nichman, T. Nieminen, J. Nowak, A. Ojdanic, A. Onnela, A. Pajunoja, T. Petäjä, F. Piel, L. L. J. Quéléver, N. Sarnela, S. Schallhart, K. Sengupta, M. Sipilä, A. Tomé, J. Tröstl, O. Väisänen, A. C. Wagner, A. Ylisirniö, Q. Zha, U. Baltensperger, K. S. Carslaw, J. Curtius, R. C. Flagan, A. Hansel, I. Riipinen, J. N. Smith, A. Virtanen, P. M. Winkler, N. M. Donahue, V.-M. Kerminen, M. Kulmala, M. Ehn, D. R. Worsnop, Size-dependent influence of $NO_x$ on the growth rates of organic aerosol particles. *Sci. Adv.* **6**, eaay4945 (2020).

37. K. Lehtipalo, C. Yan, L. Dada, F. Bianchi, M. Xiao, R. Wagner, D. Stolzenburg, L. R. Ahonen, A. Amorim, A. Baccarini, P. S. Bauer, B. Baumgartner, A. Bergen, A.-K. Bernhammer, M. Breitenlechner, S. Brilke, A. Buchholz, S. B. Mazon, D. Chen, X. Chen, A. Dias, J. Dommen, D. C. Draper, J. Duplissy, M. Ehn, H. Finkenzeller, L. Fischer, C. Frege, C. Fuchs, O. Garmash, H. Gordon, J. Hakala, X. He, L. Heikkinen, M. Heinritzi, J. C. Helm, V. Hofbauer, C. R. Hoyle, T. Jokinen, J. Kangasluoma, V.-M. Kerminen, C. Kim, J. Kirkby, J. Kontkanen, A. Kürten, M. J. Lawler, H. Mai, S. Mathot, R. L. Mauldin, U. M. III, L. Nichman, W. Nie, T. Nieminen, A. Ojdanic, A. Onnela, M. Passananti, T. Petäjä, F. Piel, V. Pospisilova, L. L. J. Quéléver, M. P. Rissanen, C. Rose, N. Sarnela, S. Schallhart, S. Schuchmann, K. Sengupta, M. Simon, M. Sipilä, C. Tauber, A. Tomé, J. Tröstl, O. Väisänen, A. L. Vogel, R. Volkamer, A. C. Wagner, M. Wang, L. Weitz, D. Wimmer, P. Ye, A. Ylisirniö, Q. Zha, K. S. Carslaw, J. Curtius, N. M. Donahue, R. C. Flagan, A. Hansel, I. Riipinen, A. Virtanen, P. M. Winkler, U. Baltensperger, M. Kulmala, D. R. Worsnop, Multicomponent new particle formation from sulfuric acid, ammonia, and biogenic vapors. *Sci. Adv.* **4**, eaau5363 (2018).

38. Q. Ye, M. Wang, V. Hofbauer, D. Stolzenburg, D. Chen, M. Schervish, A. Vogel, R. L. Mauldin, R. Baalbaki, S. Brilke, L. Dada, A. Dias, J. Duplissy, I. el Haddad, H. Finkenzeller, L. Fischer, X. He, C. Kim, A. Kürten, H. Lamkaddam, C. P. Lee, K. Lehtipalo, M. Leiminger, H. E. Manninen, R. Marten, B. Mentler, E. Partoll, T. Petäjä, M. Rissanen, S. Schobesberger, S. Schuchmann, M. Simon, Y. J. Tham, M. Vazquez-Pufleau, A. C. Wagner, Y. Wang, Y. Wu, M. Xiao, U. Baltensperger, J. Curtius, R. Flagan, J. Kirkby, M. Kulmala, R. Volkamer, P. M. Winkler, D. Worsnop, N. M. Donahue, Molecular composition and volatility of nucleated particles from α-pinene oxidation between −50 °C and +25 °C. *Environ. Sci. Technol.* **53**, 12357–12365 (2019).

39. A. Tasoglou, S. N. Pandis, Formation and chemical aging of secondary organic aerosol during the β-caryophyllene oxidation. *Atmos. Chem. Phys.* **15**, 6035–6046 (2015).

40. A. Lee, A. H. Goldstein, M. D. Keywood, S. Gao, V. Varutbangkul, R. Bahreini, N. L. Ng, R. C. Flagan, J. H. Seinfeld, Gas-phase products and secondary aerosol yields from the ozonolysis of ten different terpenes. *J. Geophys. Res. Atmos.* **111**, 10.1029/2005JD006437, (2006).

41. T. Nieminen, K. E. J. Lehtinen, M. Kulmala, Sub-10 nm particle growth by vapor condensation—Effects of vapor molecule size and particle thermal speed. *Atmos. Chem. Phys.* **10**, 9773–9779 (2010).

42. C. Deng, Y. Fu, L. Dada, C. Yan, R. Cai, D. Yang, Y. Zhou, R. Yin, Y. Lu, X. Li, X. Qiao, X. Fan, W. Nie, J. Kontkanen, J. Kangasluoma, B. Chu, A. Ding, V. M. Kerminen, P. Paasonen, D. R. Worsnop, F. Bianchi, Y. Liu, J. Zheng, L. Wang, M. Kulmala, J. Jiang, Seasonal characteristics of new particle formation and growth in urban Beijing. *Environ. Sci. Technol.* **54**, 8547–8557 (2020).

43. B. Zhao, M. Shrivastava, N. M. Donahue, H. Gordon, M. Schervish, J. E. Shilling, R. A. Zaveri, J. Wang, M. O. Andreae, C. Zhao, B. Gaudet, Y. Liu, J. Fan, J. D. Fast, High concentration of ultrafine particles in the Amazon free troposphere produced by organic new particle formation. *Proc. Natl. Acad. Sci. U.S.A.* **117**, 25344–25351 (2020).

44. M. O. Andreae, A. Afchine, R. Albrecht, B. A. Holanda, P. Artaxo, H. M. J. Barbosa, S. Borrmann, M. A. Cecchini, A. Costa, M. Dollner, D. Fütterer, E. Järvinen, T. Jurkat, T. Klimach, T. Konemann, C. Knote, M. Krämer, T. Krisna, L. A. T. Machado, S. Mertes, A. Minikin, C. Pöhlker, M. L. Pöhlker, U. Pöschl, D. Rosenfeld, D. Sauer, H. Schlager, M. Schnaiter, J. Schneider, C. Schulz, A. Spanu, V. B. Sperling, C. Voigt, A. Walser, J. Wang, B. Weinzierl, M. Wendisch, H. Ziereis, Aerosol characteristics and particle production in the upper troposphere over the Amazon Basin. *Atmos. Chem. Phys.* **18**, 921–961 (2018).

45. M. B. Enghoff, J. O. P. Pedersen, U. I. Uggerhøj, S. M. Paling, H. Svensmark, Aerosol nucleation induced by a high energy particle beam. *Geophys. Res. Lett.* **38**, 10.1029/2011GL047036, (2011).

46. J. Vanhanen, J. Mikkilä, K. Lehtipalo, M. Sipilä, H. E. Manninen, E. Siivola, T. Petäjä, M. Kulmala, Particle size magnifier for nano-CN detection. *Aerosol Sci. Tech.* **45**, 533–542 (2011).

47. K. Lehtipalo, L. R. Ahonen, R. Baalbaki, J. Sulo, T. Chan, T. Laurila, L. Dada, J. Duplissy, E. Miettinen, J. Vanhanen, J. Kangasluoma, M. Kulmala, T. Petäjä, T. Jokinen, The standard operating procedure for airmodus particle size magnifier and nano-condensation nucleus counter. *J. Aerosol Sci.* **159**, 105896 (2022).

48. D. Stolzenburg, G. Steiner, P. M. Winkler, A DMA-train for precision measurement of sub-10 nm aerosol dynamics. *Atmos. Meas. Tech.* **10**, 1639–1651 (2017).

49. S. Mirme, A. Mirme, The mathematical principles and design of the NAIS—A spectrometer for the measurement of cluster ion and nanometer aerosol size distributions. *Atmos. Meas. Tech.* **6**, 1061–1071 (2013).

50. A. Kurten, T. Jokinen, M. Simon, M. Sipilä, N. Sarnela, H. Junninen, A. Adamov, J. Almeida, A. Amorim, F. Bianchi, M. Breitenlechner, J. Dommen, N. M. Donahue, J. Duplissy, S. Ehrhart, R. C. Flagan, A. Franchin, J. Hakala, A. Hansel, M. Heinritzi, M. Hutterli, J. Kangasluoma, J. Kirkby, A. Laaksonen, K. Lehtipalo, M. Leiminger, V. Makhmutov, S. Mathot, A. Onnela, T. Petäjä, A. P. Praplan, F. Riccobono, M. P. Rissanen, L. Rondo, S. Schobesberger, J. H. Seinfeld, G. Steiner, A. Tomé, J. Tröstl, P. M. Winkler, C. Williamson, D. Wimmer, P. Ye, U. Baltensperger, K. S. Carslaw, M. Kulmala, D. R. Worsnop, J. Curtius, Neutral molecular cluster formation of sulfuric acid-dimethylamine observed in real time under atmospheric conditions. *Proc. Natl. Acad. Sci. U.S.A.* **111**, 15019–15024 (2014).

51. F. L. Eisele, D. J. Tanner, Measurement of the gas phase concentration of H2SO4and methane sulfonic acid and estimates of $H_2SO_4$ production and loss in the atmosphere. *J. Geophys. Res. Atmos.* **98**, 9001–9010 (1993).

52. A. Kürten, L. Rondo, S. Ehrhart, J. Curtius, Calibration of a chemical ionization mass spectrometer for the measurement of gaseous sulfuric acid. *J. Phys. Chem.* **116**, 6375–6386 (2012).

53. M. Ehn, E. Kleist, H. Junninen, T. Petäjä, G. Lönn, S. Schobesberger, M. Dal Maso, A. Trimborn, M. Kulmala, D. R. Worsnop, A. Wahner, J. Wildt, T. F. Mentel, Gas phase formation of extremely oxidized pinene reaction products in chamber and ambient air. *Atmos. Chem. Phys.* **12**, 5113–5127 (2012).

54. M. Heinritzi, M. Simon, G. Steiner, A. C. Wagner, A. Kürten, A. Hansel, J. Curtius, Characterization of the mass-dependent transmission efficiency of a CIMS. *Atmos. Meas. Tech.* **9**, 1449–1460 (2016).

55. M. Riva, L. Heikkinen, D. M. Bell, O. Peräkylä, Q. Zha, S. Schallhart, M. P. Rissanen, D. Imre, T. Petäjä, J. A. Thornton, A. Zelenyuk, M. Ehn, Chemical transformations in monoterpene-derived organic aerosol enhanced by inorganic composition. *npj Clim Atmos Sci* **2**, 2 (2019).

56. M. Breitenlechner, L. Fischer, M. Hainer, M. Heinritzi, J. Curtius, A. Hansel, PTR3: An instrument for studying the lifecycle of reactive organic carbon in the atmosphere. *Anal. Chem.* **89**, 5824–5831 (2017).

57. M. Riva, P. Rantala, J. E. Krechmer, O. Peräkylä, Y. Zhang, L. Heikkinen, O. Garmash, C. Yan, M. Kulmala, D. Worsnop, M. Ehn, Evaluating the performance of five different chemical ionization techniques for detecting gaseous oxygenated organic species. *Atmos. Meas. Tech.* **12**, 2403–2421 (2019).

58. F. D. Lopez-Hilfiker, C. Mohr, M. Ehn, F. Rubach, E. Kleist, J. Wildt, T. F. Mentel, A. Lutz, M. Hallquist, D. Worsnop, J. A. Thornton, A novel method for online analysis of gas and particle composition: Description and evaluation of a Filter Inlet for Gases and AEROsols (FIGAERO). *Atmos. Meas. Tech.* **7**, 983–1001 (2014).

59. H. Stark, R. L. N. Yatavelli, S. L. Thompson, H. Kang, J. E. Krechmer, J. R. Kimmel, B. B. Palm, W. Hu, P. L. Hayes, D. A. Day, P. Campuzano-Jost, M. R. Canagaratna, J. T. Jayne, D. R. Worsnop, J. L. Jimenez, Impact of thermal decomposition on thermal desorption instruments: Advantage of thermogram analysis for quantifying volatility distributions of organic species. *Environ. Sci. Technol.* **51**, 8491–8500 (2017).

60. M. Wang, D. Chen, M. Xiao, Q. Ye, D. Stolzenburg, V. Hofbauer, P. Ye, A. L. Vogel, R. L. Mauldin III, A. Amorim, A. Baccarini, B. Baumgartner, S. Brilke, L. Dada, A. Dias, J. Duplissy, H. Finkenzeller, O. Garmash, X. C. He, C. R. Hoyle, C. Kim, A. Kvashnin, K. Lehtipalo, L. Fischer, U. Molteni, T. Petäjä, V. Pospisilova, L. L. J. Quéléver, M. Rissanen, M. Simon, C. Tauber, A. Tomé, A. C. Wagner, L. Weitz, R. Volkamer, P. M. Winkler, J. Kirkby, D. R. Worsnop, M. Kulmala, U. Baltensperger, J. Dommen, I. el-Haddad, N. M. Donahue, Photo-oxidation of aromatic hydrocarbons produces low-volatility organic compounds. *Environ. Sci. Technol.* **54**, 7911–7921 (2020).

61. M. Wang, L. Yao, J. Zheng, X. K. Wang, J. M. Chen, X. Yang, D. R. Worsnop, N. M. Donahue, L. Wang, Reactions of atmospheric particulate stabilized criegee intermediates lead to high-molecular-weight aerosol components. *Environ. Sci. Technol.* **50**, 5702–5710 (2016).

62. D. W. Fahey, R. S. Gao, O. Möhler, H. Saathoff, C. Schiller, V. Ebert, M. Krämer, T. Peter, N. Amarouche, L. M. Avallone, R. Bauer, Z. Bozóki, L. E. Christensen, S. M. Davis, C. Durry, C. Dyroff, R. L. Herman, S. Hunsmann, S. M. Khaykin, P. Mackrodt, J. Meyer, J. B. Smith, N. Spelten, R. F. Troy, H. Vömel, S. Wagner, F. G. Wienhold, The AquaVIT-1 intercomparison of atmospheric water vapor measurement techniques. *Atmos. Meas. Tech.* **7**, 3177–3213 (2014).

63. A. Dias, S. Ehrhart, A. Vogel, C. Williamson, J. Almeida, J. Kirkby, S. Mathot, S. Mumford, A. Onnela, Temperature uniformity in the CERN CLOUD chamber. *Atmos. Meas. Tech.* **10**, 5075–5088 (2017).

64. J. F. Pankow, W. E. Asher, SIMPOL.1: A simple group contribution method for predicting vapor pressures and enthalpies of vaporization of multifunctional organic compounds. *Atmos. Chem. Phys.* **8**, 2773–2796 (2008).

65. D. Stolzenburg, M. Wang, M. Schervish, N. M. Donahue, Tutorial: Dynamic organic growth modeling with a volatility basis set. *J. Aerosol Sci.* **166**, 106063 (2022).

66. N. M. Donahue, S. A. Epstein, S. N. Pandis, A. L. Robinson, A two-dimensional volatility basis set: 1. Organic-aerosol mixing thermodynamics. *Atmos. Chem. Phys.* **11**, 3303–3318 (2011).

67. T. Kurtén, K. Tiusanen, P. Roldin, M. Rissanen, J.-N. Luy, M. Boy, M. Ehn, N. Donahue, α-Pinene autoxidation products may not have extremely low saturation vapor pressures despite high O:C ratios. *J. Phys. Chem.* **120**, 2569–2582 (2016).

68. C. Mohr, J. A. Thornton, A. Heitto, F. D. Lopez-Hilfiker, A. Lutz, I. Riipinen, J. Hong, N. M. Donahue, M. Hallquist, T. Petäjä, M. Kulmala, T. Yli-Juuti, Molecular identification of organic vapors driving atmospheric nanoparticle growth. *Nat. Commun.* **10**, 4442 (2019).

69. L. Dada, K. Lehtipalo, J. Kontkanen, T. Nieminen, R. Baalbaki, L. Ahonen, J. Duplissy, C. Yan, B. Chu, T. Petäjä, K. Lehtinen, V. M. Kerminen, M. Kulmala, J. Kangasluoma, Formation and growth of sub-3-nm aerosol particles in experimental chambers. *Nat. Protoc.* **15**, 1013–1040 (2020).

70. J. H. Seinfeld, S. Pandis, *Atmospheric Chemistry and Physics: From Air Pollution to Climate Change* (John Wiley & Sons, ed. 3, 2016).

71. M. Ozon, D. Stolzenburg, L. Dada, A. Seppänen, K. E. J. Lehtinen, Aerosol formation and growth rates from chamber experiments using Kalman smoothing. *Atmos. Chem. Phys.* **21**, 12595–12611 (2021).

72. M. Xiao, C. R. Hoyle, L. Dada, D. Stolzenburg, A. Kürten, M. Wang, H. Lamkaddam, O. Garmash, B. Mentler, U. Molteni, A. Baccarini, M. Simon, X. C. He, K. Lehtipalo, L. R. Ahonen, R. Baalbaki, P. S. Bauer, L. Beck, D. Bell, F. Bianchi, S. Brilke, D. Chen, R. Chiu, A. Dias, J. Duplissy, H. Finkenzeller, H. Gordon, V. Hofbauer, C. Kim, T. K. Koenig, J. Lampilahti, C. P. Lee, Z. Li, H. Mai, V. Makhmutov, H. E. Manninen, R. Marten, S. Mathot, R. L. Mauldin, W. Nie, A. Onnela, E. Partoll, T. Petäjä, J. Pfeifer, V. Pospisilova, L. L. J. Quéléver, M. Rissanen, S. Schobesberger, S. Schuchmann, Y. Stozhkov, C. Tauber, Y. J. Tham, A. Tomé, M. Vazquez-Pufleau, A. C. Wagner, R. Wagner, Y. Wang, L. Weitz, D. Wimmer, M. Wu, C. Yan, P. Ye, Q. Ye, Q. Zha, X. Zhou, A. Amorim, K. Carslaw, J. Curtius, A. Hansel, R. Volkamer, P. M. Winkler, R. C. Flagan, M. Kulmala, D. R. Worsnop, J. Kirkby, N. M. Donahue, U. Baltensperger, I. el Haddad, J. Dommen, The driving factors of new particle formation and growth in the polluted boundary layer. *Atmos. Chem. Phys.* **21**, 14275–14291 (2021).

73. R. Marten, M. Xiao, B. Rörup, M. Wang, W. Kong, X. C. He, D. Stolzenburg, J. Pfeifer, G. Marie, D. S. Wang, W. Scholz, A. Baccarini, C. P. Lee, A. Amorim, R. Baalbaki, D. M. Bell, B. Bertozzi, L. Caudillo, B. Chu, L. Dada, J. Duplissy, H. Finkenzeller, L. G. Carracedo, M. Granzin, A. Hansel, M. Heinritzi, V. Hofbauer, D. Kemppainen, A. Kürten, M. Lampimäki, K. Lehtipalo, V. Makhmutov, H. E. Manninen, B. Mentler, T. Petäjä, M. Philippov, J. Shen, M. Simon, Y. Stozhkov, A. Tomé, A. C. Wagner, Y. Wang, S. K. Weber, Y. Wu, M. Zauner-Wieczorek, J. Curtius, M. Kulmala, O. Möhler, R. Volkamer, P. M. Winkler, D. R. Worsnop, J. Dommen, R. C. Flagan, J. Kirkby, N. M. Donahue, H. Lamkaddam, U. Baltensperger, I. el Haddad, Survival of newly formed particles in haze conditions. *Environ. Sci. Atmos.* **2**, 491–499 (2022).

74. S. Iyer, M. P. Rissanen, R. Valiev, S. Barua, J. E. Krechmer, J. Thornton, M. Ehn, T. Kurtén, Molecular mechanism for rapid autoxidation in α-pinene ozonolysis. *Nat. Commun.* **12**, 878 (2021).

75. K. H. Møller, R. V. Otkjær, J. Chen, H. G. Kjaergaard, Double bonds are key to fast unimolecular reactivity in first-generation monoterpene hydroxy peroxy radicals. *J. Phys. Chem. A* **124**, 2885–2896 (2020).

76. M. P. Rissanen, T. Kurtén, M. Sipilä, J. A. Thornton, J. Kangasluoma, N. Sarnela, H. Junninen, S. Jørgensen, S. Schallhart, M. K. Kajos, R. Taipale, M. Springer, T. F. Mentel, T. Ruuskanen, T. Petäjä, D. R. Worsnop, H. G. Kjaergaard, M. Ehn, The formation of highly oxidized multifunctional products in the ozonolysis of cyclohexene. *J. Am. Chem. Soc.* **136**, 15596–15606 (2014).

# Role of sesquiterpenes in biogenic new particle formation

Lubna Dada, Dominik Stolzenburg, Mario Simon, Lukas Fischer, Martin Heinritzi, Mingyi Wang, Mao Xiao, Alexander L. Vogel, Lauri Ahonen, Antonio Amorim, Rima Baalbaki, Andrea Baccarini, Urs Baltensperger, Federico Bianchi, Kaspar R. Daellenbach, Jenna DeVivo, Antonio Dias, Josef Dommen, Jonathan Duplissy, Henning Finkenzeller, Armin Hansel, Xu-Cheng He, Victoria Hofbauer, Christopher R. Hoyle, Juha Kangasluoma, Changhyuk Kim, Andreas Kürten, Aleksander Kvashnin, Roy Mauldin, Vladimir Makhmutov, Ruby Marten, Bernhard Mentler, Wei Nie, Tuukka Petäjä, Lauriane L. J. Quéléver, Harald Saathoff, Christian Tauber, Antonio Tome, Ugo Molteni, Rainer Volkamer, Robert Wagner, Andrea C. Wagner, Daniela Wimmer, Paul M. Winkler, Chao Yan, Qiaozhi Zha, Matti Rissanen, Hamish Gordon, Joachim Curtius, Douglas R. Worsnop, Katrianne Lehtipalo, Neil M. Donahue, Jasper Kirkby, Imad El Haddad, and Markku Kulmala

**View the article online**
https://www.science.org/doi/10.1126/sciadv.adi5297
**Permissions**
https://www.science.org/help/reprints-and-permissions

Use of this article is subject to the Terms of service